Cell Stem Cell

Clinical and Translational Report

Nanoengineered 3D culture substrate enables superior persistence and polyclonal engraftment of genetically engineered hematopoietic stem cells

Graphical abstract

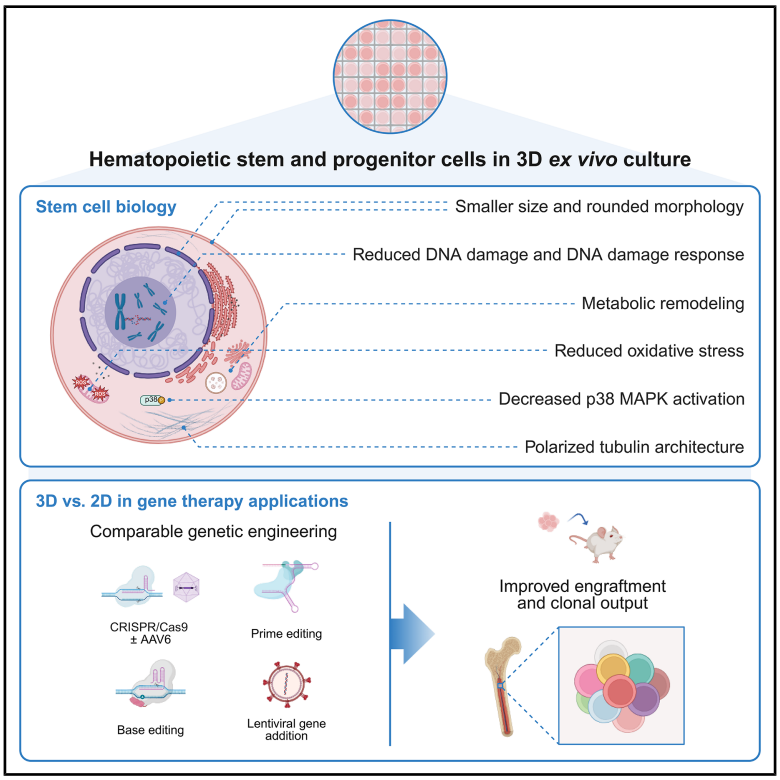

Highlights

- 3D cues profoundly rewire HSPC transcriptional profile during *ex vivo* manipulation
- Cytoskeletal and nuclear architecture regulate HSPC properties and functionality
- Nichoids enable efficient genetic engineering across multiple platforms
- 3D culture enhances persistence and clonal output of genetically engineered cells

Authors

Federico Midena, Laura Alessandrini, Claudio Conci, ..., Eugenio Montini, Manuela T. Raimondi, Raffaella Di Micco

Correspondence

dimicco.raffaella@hsr.it

In brief

Preserving the functionality of hematopoietic stem cells during *ex vivo* manipulation for clinical applications remains a challenge. Here, Midena et al. implement a nanoengineered 3D culture substrate compatible with multiple gene therapy platforms that enhances the engraftment and clonal output of engineered cells through biomechanical regulation of stem cell properties.

Midena et al., 2026, Cell Stem Cell *33*, 217–232
February 5, 2026
https://doi.org/10.1016/j.stem.2025.12.016

CellPress

Cell Stem Cell

CellPress
OPEN ACCESS

Clinical and Translational Report

Nanoengineered 3D culture substrate enables superior persistence and polyclonal engraftment of genetically engineered hematopoietic stem cells

Federico Midena,[1,2] Laura Alessandrini,[1,2] Claudio Conci,[3] Matteo Barcella,[1] Francesco Gazzo,[1,4] Emanuela Jacchetti,[3] Edoardo Carsana,[1] Fabrizio Benedicenti,[1] Roberta Vacca,[1,2] Lucrezia della Volpe,[1] Sergio Arévalo,[1] Kety Giannetti,[1] Dafne Barozzi,[5] Martina Franchino,[2,5] Erika Zonari,[1] Francesca Ferrua,[1,6] Giacomo Farina,[1,7] Chiara Brombin,[8] Federica Cugnata,[8] Martina Fiumara,[1] Teresa Tavella,[1] Leonardo Cherubin,[3] Federico Fraschetta,[6] Giulio Cerullo,[9,10] Roberto Osellame,[10] Marina Radrizzani,[1] Samuele Ferrari,[1] Ivan Merelli,[1,11] Bernhard Gentner,[1,12] Cristina Scielzo,[5] Andrea Brendolan,[5] Luigi Naldini,[1,2] Alessandro Aiuti,[1,2,6] Eugenio Montini,[1] Manuela T. Raimondi,[3] and Raffaella Di Micco[1,13,14,*]

[1]San Raffaele Telethon Institute for Gene Therapy (SR-Tiget), IRCCS San Raffaele Scientific Institute, 20132 Milan, Italy
[2]Vita-Salute San Raffaele University, 20132 Milan, Italy
[3]Department of Chemistry, Materials, and Chemical Engineering "Giulio Natta," Politecnico di Milano, 20133 Milan, Italy
[4]Department of Electronics, Information, and Bioengineering, Politecnico di Milano, 20133 Milan, Italy
[5]Division of Experimental Oncology, IRCCS San Raffaele Scientific Institute, 20132 Milan, Italy
[6]Pediatric Immunohematology and Bone Marrow Transplantation Unit, IRCCS San Raffaele Scientific Institute, 20132 Milan, Italy
[7]University of Milan-Bicocca, 20126 Milan, Italy
[8]CUSSB - University Center for Statistics in the Biomedical Sciences, Vita-Salute San Raffaele University, 20132 Milan, Italy
[9]Department of Physics, Politecnico di Milano, 20133 Milan, Italy
[10]National Research Council, Institute for Photonics and Nanotechnologies (IFN-CNR), 20133 Milan, Italy
[11]National Research Council, Institute for Biomedical Technologies, 20054 Segrate, Italy
[12]Ludwig Institute for Cancer Research and Department of Oncology, University of Lausanne (UNIL) and Lausanne University Hospital (CHUV), 1011 Lausanne, Switzerland
[13]University School of Advanced Studies IUSS, 27100 Pavia, Italy
[14]Lead contact
*Correspondence: dimicco.raffaella@hsr.it
https://doi.org/10.1016/j.stem.2025.12.016

SUMMARY

Ex vivo culture of hematopoietic stem and progenitor cells (HSPCs) is required for gene therapy applications but inadvertently triggers detrimental cellular responses, potentially threatening clinical success. In this study, we employ nichoids, biocompatible 3D culture substrates with cell-scale resolution, to provide HSPCs with mechanical support during *ex vivo* manipulation. This innovative 3D system improves HSPC multi-lineage differentiation and engraftment capacity by leveraging mechanobiological control over nuclear morphology, cytoskeleton organization, metabolism, and DNA integrity. Notably, 3D culture enables efficient genetic engineering across multiple platforms, including long-range gene editing, base- and prime-editing, and lentiviral-mediated gene addition. Moreover, this scaffold increases the clonal output and persistence of genetically engineered cells in xenotransplantation experiments, including a clinical protocol for lentiviral gene addition in Wiskott-Aldrich syndrome. Overall, we propose a transformative approach to enhance the efficacy and safety of emerging and established hematopoietic stem cell-based gene therapy applications.

INTRODUCTION

Autologous hematopoietic stem and progenitor cell (HSPC)-based gene therapies (GTs) offer a promising one-and-done treatment for multiple immune-hematologic and genetic diseases, including cross-correction of non-hematopoietic cells in some non-hematological disorders.[1–4] Genetic engineering of HSPCs was first achieved through semi-randomly integrating viral vectors like gamma-retroviruses and pseudotyped lentiviral vectors (LVs),[5–8] while nowadays gene editing (GE) platforms, such as CRISPR-Cas9 and base and prime editors,[9–11] can induce targeted modifications up to single-nucleotide precision. Yet, despite numerous successes in clinical trials and the market approval of some of these therapies,[6–8,12–19] considerable challenges prevent a broader adoption of these living drugs, including reaching high engineering efficiency without compromising the functionality of HSPCs, ensuring the highest predicted safety of the cell product, and managing the extremely

high research and development (R&D) and manufacturing costs.[20–22] From a biological standpoint, genetic engineering triggers various adverse reactions, including the activation of the DNA damage response (DDR) and the formation of potential genotoxic byproducts, like insertions or deletions (indels), chromosomal rearrangements, or insertional mutagenesis.[23–28] Moreover, *ex vivo* culture further induces DNA damage and oxidative stress, which rapidly reduce self-renewal potential, promote differentiation, and potentially lead to the loss of the most primitive hematopoietic stem cells (HSCs), responsible for the life-long supply of the entire hematopoietic compartment.[29–32] Altogether, these detrimental responses diminish the yield and quality of genetically engineered cells, delay hematopoietic reconstitution, and shrink the clonal repertoire of repopulating stem cells,[3,22,28,33,34] therefore raising potential efficacy and safety concerns and highlighting the long-term risk of developing clonal hematopoiesis and blood malignancies.

In current GT protocols, *ex vivo* culture is not only required for delivering the vector payload or the editing reagents but also, in some cases, to increase the number of transplantable cells. Thus, alongside the development of more efficient and precise editing tools and enhancers,[25,34–36] significant efforts are spent to advance culture conditions to ensure the maintenance, and potentially the expansion, of HSCs *ex vivo*. These include fine-tuning the supporting cytokine combinations, supplementing small molecules like nicotinamide riboside, UM171, and ferroptosis inhibitors, and introducing only chemically defined reagents to avoid batch-to-batch variability and diminish possible contaminants.[31,37–42] Yet, traditional 2D cultures are unlikely to fully recapitulate all the essential supportive elements of the endogenous HSC niche. Indeed, although the HSPC mechanobiology field is still relatively in its infancy, several studies have highlighted the critical role of 3D cues and mechanical forces in HSC specification and maintenance under both physiological and *ex vivo* conditions.[43–49] For this reason, engineered 3D culture systems represent an appealing strategy to model the architecture of the native bone marrow (BM) niche and provide mechanical support to HSCs during *ex vivo* manipulation.

Here, we implemented a biocompatible 3D culture system into multiple GT protocols, improving the persistence and clonal output of engineered cells for more effective and safer therapeutic applications.

RESULTS

3D culture increases the functionality of HSPCs upon *ex vivo* manipulation

To provide mechanical support to HSPCs during *ex vivo* culture, we tested nichoids,[50] chemically and structurally stable 3D substrates micro-fabricated with cell-scale resolution, featuring a miniaturized architecture of 10–30 × 15 μm elementary units produced through two-photon polymerization (Figure 1A). Specifically, we seeded cord blood (CB)-derived CD34+ human HSPCs either on standard culture wells (2D) or nichoids (3D) immediately after thawing and collected them after 3 or 7 days for downstream analyses (Figure 1B). To retrieve HSPCs from the scaffold, we optimized a detachment protocol using a citrate solution, which allowed us to recover 75% of the cells seeded without affecting cell viability or HSPC ability to generate colonies in the standard colony-forming unit cell (CFU-C) assay (Figures S1A–S1C; Table S1).

First, we found similar percentages of viable cells and phenotypically defined HSPC subsets between the two different culture systems (Figures 1C, S1D, and S1E). However, when testing the clonogenic potential of an equal number of cells, 3D culture significantly increased the output of mixed colonies, the progeny of more primitive and multipotent cells,[51] as well as the erythroid fraction in the first time point (Figure 1D). As nichoids are fabricated on glass supports that may affect HSPC behavior per se, we then compared standard tissue plates or glass coverslips with 3D culture. Although we found a similar increase in erythroid colonies between glass and 3D, we reported higher mixed-colony output exclusively in the nichoid condition (Figure S1F). Additionally, the improved colony output occurred only if HSPCs were seeded immediately on 3D post-thawing and not after 1 to 2 days of initial 2D culture (Figure S1G), highlighting the importance of 3D stimuli during early *ex vivo* culture adaptation.

To gather some insights on the more primitive HSPC compartment, we fluorescence-activated cell sorting (FACS) sorted HSC-enriched single cells (defined as CD34+CD133+CD90+CD45RA−) on the third day of culture and assessed their multi-lineage differentiation potential along the myeloid (My), erythroid (Ery), megakaryocytic (Meg), and natural killer (NK) branches[52] (Figure S1H). Although not statistically significant, we found a tendency toward an increased number of different lineages present within single cell-derived colonies from the 3D condition (Figure 1E). Moreover, nichoid pre-cultured cells gave rise to colonies with higher cellularity (Figure 1F), supporting enhanced functionality of the stem cell compartment upon 3D culture. In terms of lineage specification, by analyzing in detail the composition of uni-lineage and multi-lineage colonies, we found an expansion of the Ery-only and MyNK output in the 3D condition, with a proportional decrease in the fraction of My-only and EryMeg colonies (Figures S1I and S1J).

We next transplanted equal numbers of 2D or 3D cultured HSPCs into immunodeficient mice to assess their hematopoietic reconstitution potential. Importantly, we reported higher human chimerism in the peripheral blood (PB) of mice injected with nichoid-cultured HSPCs (Figure 1G), with superior engraftment across multiple hematopoietic organs, including the BM and spleen (SP) (Figures 1H and 1I). Additionally, PB analyses revealed higher fractions of myeloid and T cells present in the 3D condition (Figures S1K and S1L), while we observed similar graft composition in the BM and a modest increase in T cell output in the SP (Figures S1M and S1N). At last, we purified human CD34+ cells from the BM of the mice and found a higher clonogenic output of nichoid pre-cultured HSPCs upon further re-challenging in the CFU-C assay (Figure 1J).

Altogether, our findings demonstrate that nichoids significantly enhance HSPC functionality compared with traditional 2D cultures, supporting a critical role of 3D cues in preserving stem cell properties during *ex vivo* manipulation.

3D culture rewires the transcriptional profile of HSPCs and preserves nuclear and cytoskeleton organization

To dissect the molecular changes dictated by nichoids, we performed transcriptional analysis on CB-derived CD34+ cells cultured in 2D or 3D at two different time points. Surprisingly,

CellPress
OPEN ACCESS

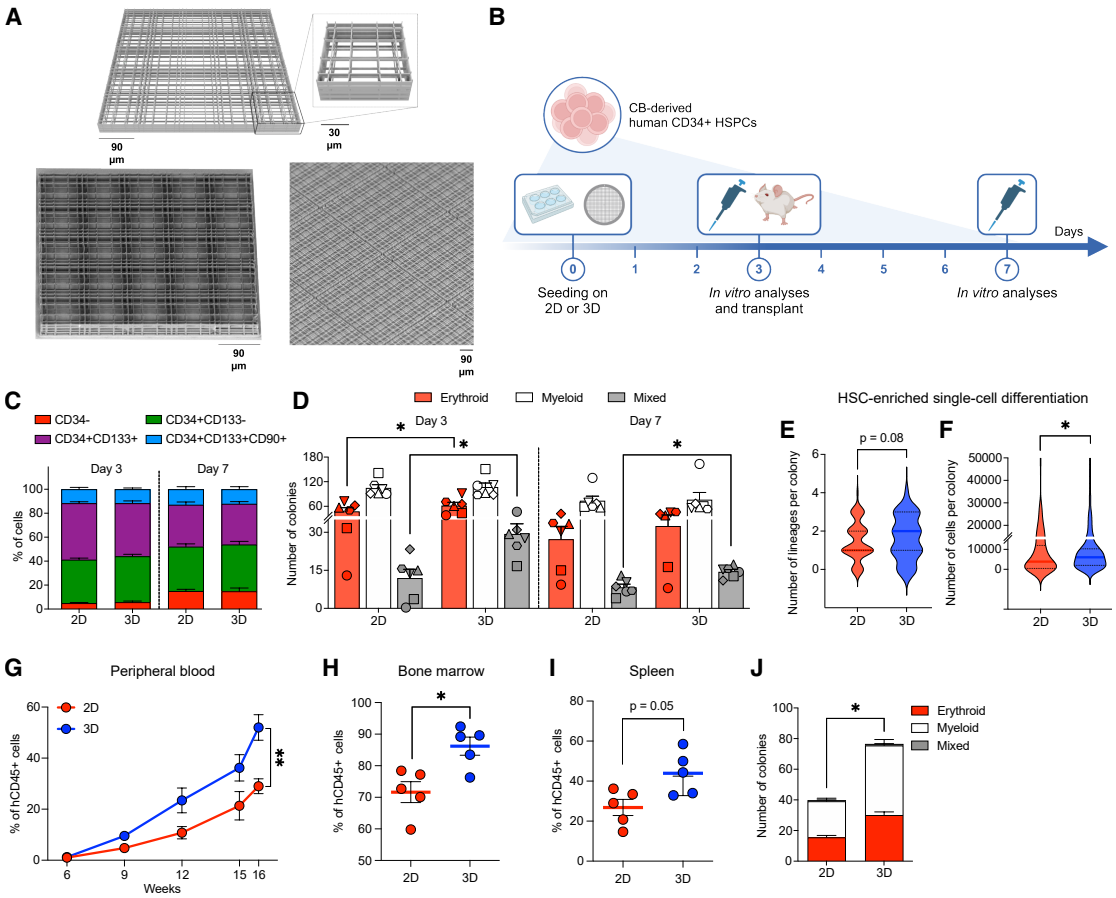

Figure 1. Nichoids improve the functionality of *ex vivo* cultured HSPCs

(A) Schematic representation with highlight of a single elementary unit (top) and scanning electron microscopy images (bottom) of the nichoid culture substrate. Scale bars: 30 or 90 µm.

(B) Experimental workflow. Human CB-derived HSPCs were seeded on 2D or nichoids immediately after thawing and collected for downstream analyses on days 3 and 7.

(C) Percentage of phenotypically defined HSPC subsets (n = 9, 9, 10, 10).

(D) Number of erythroid, myeloid, and mixed colonies generated in the CFU-C assay (n = 6). Wilcoxon test.

(E and F) Number of lineages (E) and cells (F) per colony generated by HSC-enriched single cells. More than 250 colonies were analyzed for each condition. Median ± 95% CI. Mann-Whitney test.

(G–I) Percentage of human CD45+ (hCD45+) cells measured in the PB (G) over time and BM (H) and SP (I) at the endpoint (n = 5). Mann-Whitney test (calculated at the last time point for PB).

(J) Number of erythroid, myeloid, and mixed colonies generated by BM-derived CD34+ cells purified from mice in (H) (n = 5). Mann-Whitney test.

Unless otherwise specified, mean ± SEM. *$p < 0.05$, **$p < 0.01$.

See also Figure S1 and Table S1.

nichoids induced a profound reshaping of the transcriptional profile of HSPCs, with differential modulation of 5,399 and 5,255 genes on days 4 and 7, respectively (Figure S2A). When performing gene set enrichment analysis (GSEA), we found upregulation of cellular pathways related to the extracellular matrix (ECM), cell adhesion, and cytoskeleton organization in the 3D condition, with the latter significantly modulated only at the later time point (Figure 2A; Table S2). Conversely, we reported downregulation of genes belonging to DNA replication, cell division, transcription, protein synthesis and degradation, and oxidative respiration, features associated with more primitive and dormant stem cells,[32,53–55] and DDR signaling and DNA repair (Figure 2A).

To narrow down our analysis, we focused on specific genes involved in cell adhesion, cytoskeletal rearrangements and signaling, and other HSPC-related pathways (Figure 2B). Thus, we found upregulation of multiple integrin subunits (*ITGA1*, *ITGA3*, *ITGA5*, and *ITGB1*), combined with differential modulation of microfilament and microtubule remodelers (such as *CLF1*, *CAPG*, *VIL1*, *STMN1*, and *CLIP1*), and upregulation of focal adhesion genes and GPCRs (such as *PTK2*, also known as focal adhesion kinase 1, *PAK4*, *ROCK1*, and *GPRC5C*), indicating a crosstalk between the 3D scaffold and HSPCs, conceivably through mechano-sensing. Intriguingly, we also reported downregulation of *CDC42*, a small GTPase of the Rho subfamily that regulates HSC aging and rejuvenation.[56] Moreover, we

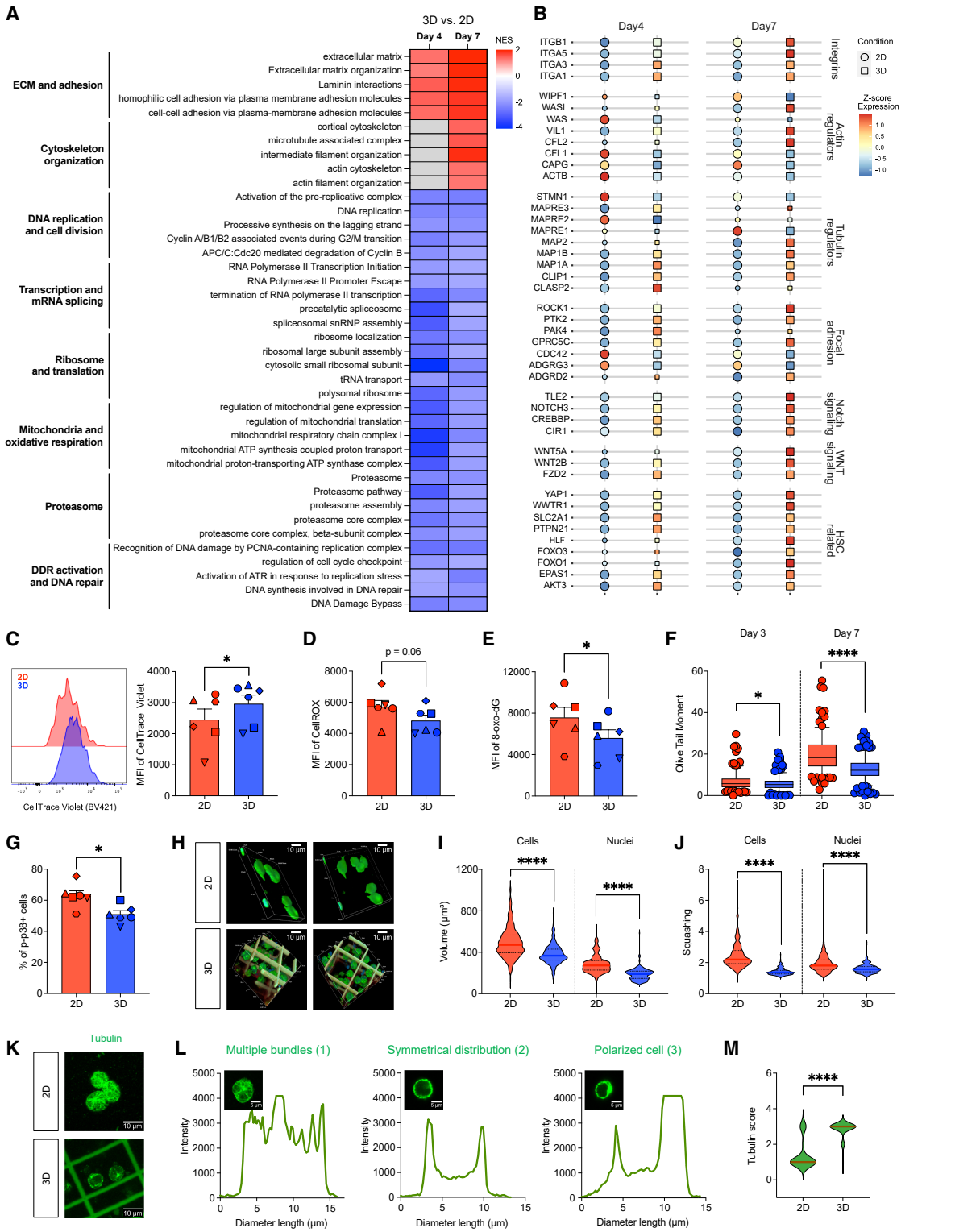

Figure 2. Nichoids profoundly rewire *ex vivo* manipulated HSPCs

(A) Differentially modulated gene categories from GSEA of 3D- vs. 2D-cultured HSPCs. The color gradient reflects the normalized enrichment score (NES), and gray boxes indicate non-significant modulation (*p*.adjust > 0.05).

(B) Average gene expression (*Z* score) for the indicated genes. Differentially expressed genes (FDR < 0.05) are represented with symbols of larger size.

(C) Representative plot (left) and median fluorescence intensity (MFI) (right) of CellTrace dye dilution in HSPCs on day 7 ($n = 6$). Wilcoxon test.

(D) MFI of ROS measured by CellROX staining in HSPCs on day 7 ($n = 6$). Wilcoxon test.

(legend continued on next page)

detected upregulations of genes of the Notch and Wnt signaling pathways (such as *NOTCH3*, *CREBBP*, *FZD2*, and *WNT5A*), *HLF*, *SLC2A1* (Glut1), *EPAS1* (Hif2a), *FOXO1* and *FOXO3*, Akt, Yap/Taz, and *PTPN21*, which are fundamental for HSC specification and maintenance.[43,48,57–67]

At this stage, we characterized nichoid-cultured HSPCs through multiple experimental analyses to validate these findings. First, we assessed cell proliferation through CellTrace dye staining and found that, while HSPCs grown on nichoids from both the bulk CD34+ and the more primitive CD34+CD133+CD90+ subsets showed similar proliferation kinetics to traditional 2D conditions in the first days of *ex vivo* culture, they cumulatively performed fewer rounds of cell division on day 7, as supported by heightened dye retention (Figures 2C, S2B, and S2C). Moreover, we reported reduced oxidative stress with decreased accumulation of reactive oxygen species (ROS) and 8-oxo-2′-deoxyguanosine (8-oxo-dG) DNA lesions (Figures 2D and 2E). In addition, the alkaline comet assay revealed fewer DNA single- and double-strand breaks in the 3D condition (Figure 2F). Accordingly, we found fewer foci of phosphorylated Replication Protein A (pRPA) and phosphorylated histone H2A.X (γH2AX), upstream mediators of DNA damage sensing and DDR activation[68] (Figure S2D). Interestingly, we also reported reduced activation of the p38 mitogen-activated protein kinase (MAPK) , which we recently identified as a crucial orchestrator of HSPC dysfunction upon *ex vivo* culture and proliferation stress[32] (Figures 2G and S2E). Of note, similar results were also observed when working with non-cryopreserved HSPCs purified from fresh CB (Figures S2F–S2J).

We then analyzed HSPC morphology in the presence of nichoids. Strikingly, we reported that 3D culture endowed *ex vivo* cultured cells with a small and spherical shape, whereas HSPCs grown on 2D were enlarged and flattened (Figure 2H). This observation was confirmed also for HSPC nuclei by measuring physical parameters like the volume and squashing (defined as the ratio between the long and short axes of each cell, where squashing values close to 1 reflect spherical objects) (Figures 2I and 2J). When performing this analysis, we also found a distinct architecture of the microtubule cytoskeleton. Specifically, 3D cultured HSPCs presented a defined tubulin organization, either polarized or equally distributed beneath the outer layer of the cell, while the 2D condition displayed multiple microtubule bundles spread across the entire cellular volume (Figure 2K). Thus, we assigned a tubulin score to single HSPCs based on the intensity of the tubulin signal along the cell diameter (1 for multiple bundles, 2 for symmetrical distribution underneath the plasma membrane, and 3 for polarized cells) (Figure 2L) and reported a distinct architecture of the microtubule cytoskeleton between the two conditions, with the majority of nichoid-cultured HSPCs with polarized tubulin distribution (Figure 2M), likely resulting from the interactions with the scaffold or the exposure to different mechanical forces between the two culture systems.

Finally, to investigate whether distinct 3D culture platforms may differentially regulate HSPC responses, we tested two alternative 3D systems, including a spongostan scaffold and a collagen-based spheroid model (Figure S3A), previously exploited in hematological cancers.[69,70] To this aim, we employed HSPCs from mobilized PB (mPB), an adult CD34+ cell source of clinical relevance.[3,71] Despite a minor decrease in cell viability in the two alternative systems (Figure S3B), which did not significantly impact HSPC subset composition (Figure S3C), we found that all 3D cultures influenced HSPC behavior, although the effects on cell proliferation, oxidative stress, DNA damage, p-p38 activation, cytoskeleton organization, and clonogenic potential varied across conditions (Figures S3D–S3J). Interestingly, only nichoids increased the output of mixed colonies, suggesting that different culture systems may ultimately induce both convergent and distinct biological responses.

Overall, nichoids induce a profound transcriptional rewiring of HSPCs, upregulating molecular pathways related to cytoskeleton remodeling and adhesion, with a concomitant decrease in cell proliferation, oxidative stress, and DNA damage accumulation. Mechanistically, nichoids prevent HSPC deformation and squashing of conventional 2D culture, preserve nuclear morphology and tubulin polarity, and potentially facilitate adaptation to *ex vivo* culture with consequent preservation of stemness properties.

3D culture allows efficient GE across multiple platforms and endows HDR-edited HSPCs with superior long-term engraftment

We then reasoned that nichoids could improve genetic engineering protocols for clinical applications, which involve additional manipulation steps that directly affect HSPC functionality.[23,24] Thus, we seeded human CB- or mPB-derived CD34+ cells on 2D or 3D and performed long-range GE according to our established Cas9/adeno-associated virus serotype 6 (AAV6) protocol[24] to achieve homology-directed repair (HDR)-mediated insertion of a GFP reporter within the *AAVS1* locus (Figure 3A). Of note, HSPCs from the 3D condition were seeded on 2D post-nucleofection for functional studies to avoid repetitive cycles of detachment and reseeding, which could increase cellular stress and diminish the quantity of available edited HSPCs.

Nichoid pre-culture did not affect the viability and the fractions of HSPC subsets, even if the GE procedure was generally less

(E) MFI of 8-oxo-dG in HSPCs on day 7 ($n = 6$). Wilcoxon test.
(F) Quantification of single-strand and double-strand breaks by alkaline comet assay, and each dot represents a single cell (more than 200 cells were analyzed for each condition). Median ± 95% CI. Mann-Whitney test.
(G) Percentage of phospho-p38 (p-p38)-positive HSPCs on day 7 ($n = 6$). Wilcoxon test.
(H) Representative 3D renderings of HSPCs on day 7 of 2D or 3D culture, obtained from immunofluorescence z-stack confocal imaging. Scale bars: 10 μm.
(I and J) Quantification of volume (I) and squashing (J) morphological parameters on day 7, and each dot represents a single cell or nucleus (more than 250 cells were analyzed for each condition). Median. Mann-Whitney test.
(K) Representative immunofluorescence showing tubulin spatial organization in HSPCs on day 7. Scale bars: 10 μm.
(L and M) Representative immunofluorescence (L) and quantification (M) of tubulin score measured along cell diameter in HSPCs on day 7 (more than 100 cells were analyzed for each condition). Median value. Mann-Whitney test. Scale bars: 5 μm.
Unless otherwise specified, mean ± SEM. $^{*}p < 0.05$, $^{****}p < 0.0001$.
See also Figures S2 and S3 and Tables S1 and S2.

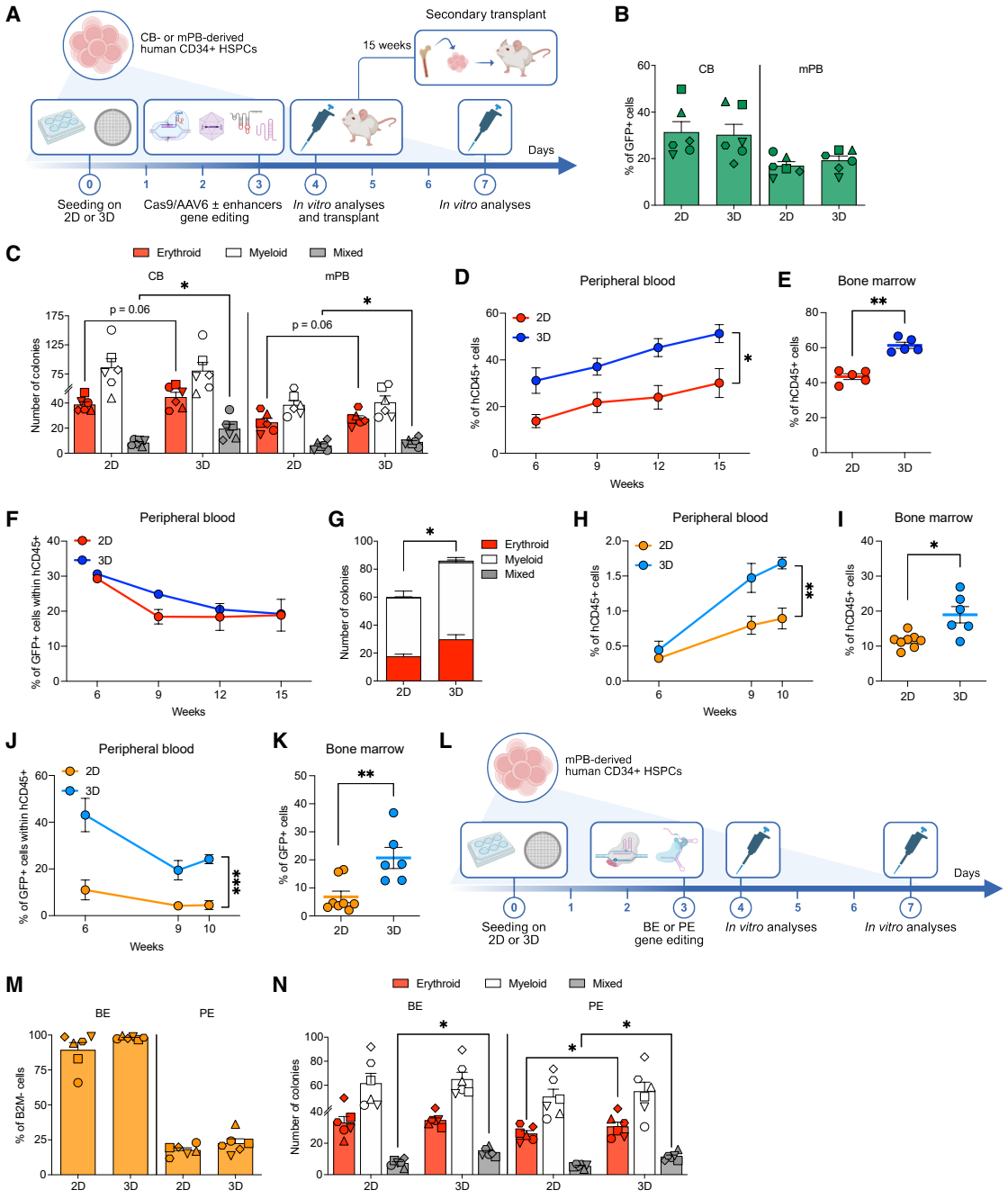

Figure 3. Nichoids enable efficient GE across multiple platforms and superior long-term engraftment of HDR-edited HSPCs

(A) Experimental workflow. Human CB- or mPB-derived HSPCs were seeded on 2D or 3D immediately after thawing and collected on day 3 for nucleofection. Specifically, cells were edited with Cas9/AAV6 alone or in the presence of GSE56 and Ad5-E4orf6/7 editing enhancers to insert a GFP reporter within the *AAVS1* locus. HSPCs from both the 2D and 3D conditions were seeded in 2D after nucleofection and collected for downstream analyses on days 4 and 7. Transplantation was performed only for the Cas9/AAV6 plus GSE56 and Ad5-E4orf6/7 editing enhancers treatment using CB-derived HSPCs. After 15 weeks post-injection, CD34+ cells were purified from the BM of the mice and transplanted into secondary recipients.

(B) Percentage of edited HSPCs by FACS analysis on day 7 ($n = 6$).

(C) Number of erythroid, myeloid, and mixed colonies generated in the CFU-C assay from edited HSPCs seeded on day 4 ($n = 6$). Wilcoxon test.

(D and E) Percentage of hCD45+ cells measured in the PB (D) over time and BM (E) at the endpoint of transplanted mice ($n = 5$). Mann-Whitney test (calculated at the last time point for PB).

(F) Percentage of GFP+ cells (within hCD45+ cells) in the PB over time from mice in (D) ($n = 5$).

(G) Number of erythroid, myeloid, and mixed colonies generated by BM-derived CD34+ cells purified from mice in (E) ($n = 5$). Mann-Whitney test.

(H and I) Percentage of hCD45+ cells measured in the PB (H) over time and BM (I) at the endpoint of transplanted secondary recipients ($n = 8, 6$). Mann-Whitney test (calculated at the last time point for PB).

(legend continued on next page)

tolerated in the mPB source (Figures S4A and S4B). Additionally, we reported comparable editing efficiencies across culture conditions in both the bulk CD34+ and the more primitive CD34+ CD133+CD90+ fractions, although lower in mPB (Figures 3B and S4C–S4E). Intriguingly, nichoid pre-culture was sufficient to slow down HSPC proliferation even upon re-plating on standard 2D culture (Figure S4F). Nonetheless, the fraction of cells in the HDR-permissive S/G2 cell cycle phases at the time of nucleofection was similar between culture conditions (Figure S4G), thus explaining the comparable editing levels. Importantly, nichoids improved the mixed-colony output of edited cells, with a slight increment also in the erythroid fraction (Figure 3C).

We then assessed the repopulating potential of edited HSPCs. To this aim, we exploited two validated and transiently expressed editing enhancers, a dominant-negative p53 variant (GSE56) to counteract GE-induced DDR activation and an adenoviral helper protein (Ad5-E4orf6/7) to favor HDR engagement[24] (Figures 3A and S4H–S4L). We found higher human chimerism in the PB, BM, and SP of mice from the nichoid group (Figures 3D, 3E, and S5A), with comparable levels of HDR-edited cells, assessed by both GFP expression and molecular analysis (Figures 3F and S5B–S5E), and graft composition (Figures S5F–S5H) between the two conditions. Moreover, nichoid pre-cultured CD34+ cells recovered from the mice maintained a higher clonogenic potential (Figure 3G). At this stage, we then specifically challenged long-term HSCs by injecting BM-derived CD34+ cells from primary mice into secondary recipients. Strikingly, we reported higher engraftment in the 3D group across all the hematopoietic organs (Figures 3H, 3I, and S5I), with a three- to six-fold increase in the percentage of HDR-edited cells (Figures 3J, 3K, S5J, and S5K) and similar graft composition compared with the 2D group (Figures S5L–S5N), confirming the beneficial effects of nichoid for preserving functional stem cells upon genetic manipulation.

Finally, we observed similar *in vitro* results also when performing base and prime editing (BE and PE, respectively) in mPB-derived HSPCs using optimized mRNAs encoding for an adenine base editor (ABE8.20-m) or prime editor (PE3max)[25] to knock out (KO) the *B2M* gene (Figures 3L–3N and S5O–S5U).

Collectively, nichoids enable efficient GE and enhance the functionality of edited HSPCs across multiple platforms, including Cas9/AAV6, BE, and PE. Moreover, 3D culture improves the long-term reconstitution of engineered HSPCs, increasing the persistence of HDR-edited cells through serial transplantation.

3D culture increases the clonal output of repopulating HSPCs upon lentiviral gene addition

As most market-approved and late-stage development HSPC-GTs rely on LV-mediated gene addition, we tested whether nichoids could further advance these protocols. Upon a 24 h *ex vivo* pre-stimulation, we performed LV transduction of mPB-derived CD34+ cells in 2D or directly on nichoids, in the presence of 16,16-dimethyl prostaglandin E2 (PGE2) alone[15,37] or in combination with the transduction-enhancer cyclosporine H (CsH),[35] to achieve LV-mediated insertion of a GFP reporter (Figure 4A).

As expected, cell viability was not affected by CsH administration and was similar between the two culture conditions (Figure S6A). Moreover, while we reported a comparable fraction of transduced cells across subsets (Figures 4B and S6B) and vector copy number (VCN) (Figure S6C) in 2D or 3D, CsH allowed reaching saturating levels of GFP+ cells even at lower LV multiplicity of infection (MOI) (30 vs. 100). Notably, nichoids improved the erythroid and mixed-colony-forming potential of transduced cells, even in the presence of CsH, which did not affect HSPC clonogenic output per se (Figure 4C).

To validate these findings, we transplanted cells transduced with CsH and found higher human chimerism in the PB, BM, and SP from mice of the nichoid group (Figures 4D, 4E, and S6D). Of note, almost the entire grafts were composed of GFP+ cells (Figures 4F, S6E, and S6F). Additionally, 3D culture increased the T cell output in the PB of the mice (Figure S6G), while we observed a similar composition to the 2D condition in the BM and SP (Figures S6H and S6I). Moreover, BM-derived CD34+ cells from the 3D group maintained a higher clonogenic potential when challenged in the CFU-C assay (Figure 4G), indicating that even a brief period of *ex vivo* culture as short as 36h on nichoids can benefit the functionality of HSPCs in long-term experiments.

To further characterize the efficacy and safety of 3D culture in LV-based GT approaches, we also monitored the clonal dynamics of engrafting HSPCs through integration site (IS) analyses.[8,72] We retrieved a high number of unique integrations across the PB, BM, and BM-purified CD34+ cells of both conditions, which were generally more abundant in the 3D group (Figure S6J). In line with the relatively short half-life of most hematopoietic progenitors supporting the early engraftment phase, we found only a moderate persistence of PB-repopulating clones over time, while we observed the highest clonal sharing between the BM and BM-derived CD34+ HSPCs at the endpoint (Figures 4H and S6K). Importantly, no clonal expansion events were reported in any of the mice (Figures 4H and S6K). Focusing on the complexity of the clonal repertoire, we then estimated population size and diversity by normalizing the number of unique integrations and the Shannon diversity index on the VCN. Thus, we found a higher number of engrafting clones and improved clonal diversity in the 3D condition (Figures 4I and 4J), indicating that nichoids better preserved the fraction of HSPCs capable of reconstituting the hematopoietic system. Finally, gene targeting frequency analyses confirmed no

(J and K) Percentage of GFP+ cells (within hCD45+ cells) in the PB (J) over time and BM (K) from mice in (H and I) (n = 8, 6). Mann-Whitney test (calculated at the last time point for PB).

(L) Experimental workflow. Human mPB-derived HSPCs were seeded on 2D or 3D immediately after thawing and collected on day 3 for nucleofection. Specifically, cells were edited with BE or PE to disrupt the *B2M* gene. HSPCs from both the 2D and 3D conditions were seeded in 2D after nucleofection and collected for downstream analyses on days 4 and 7.

(M) Percentage of edited HSPCs by FACS analysis on day 7 (n = 6).

(N) Number of erythroid, myeloid, and mixed colonies generated in the CFU-C assay from edited HSPCs seeded on day 4 (n = 6). Wilcoxon test.

Mean ± SEM. *p < 0.05, **p < 0.01, ***p < 0.001.

See also Figures S4 and S5 and Table S1.

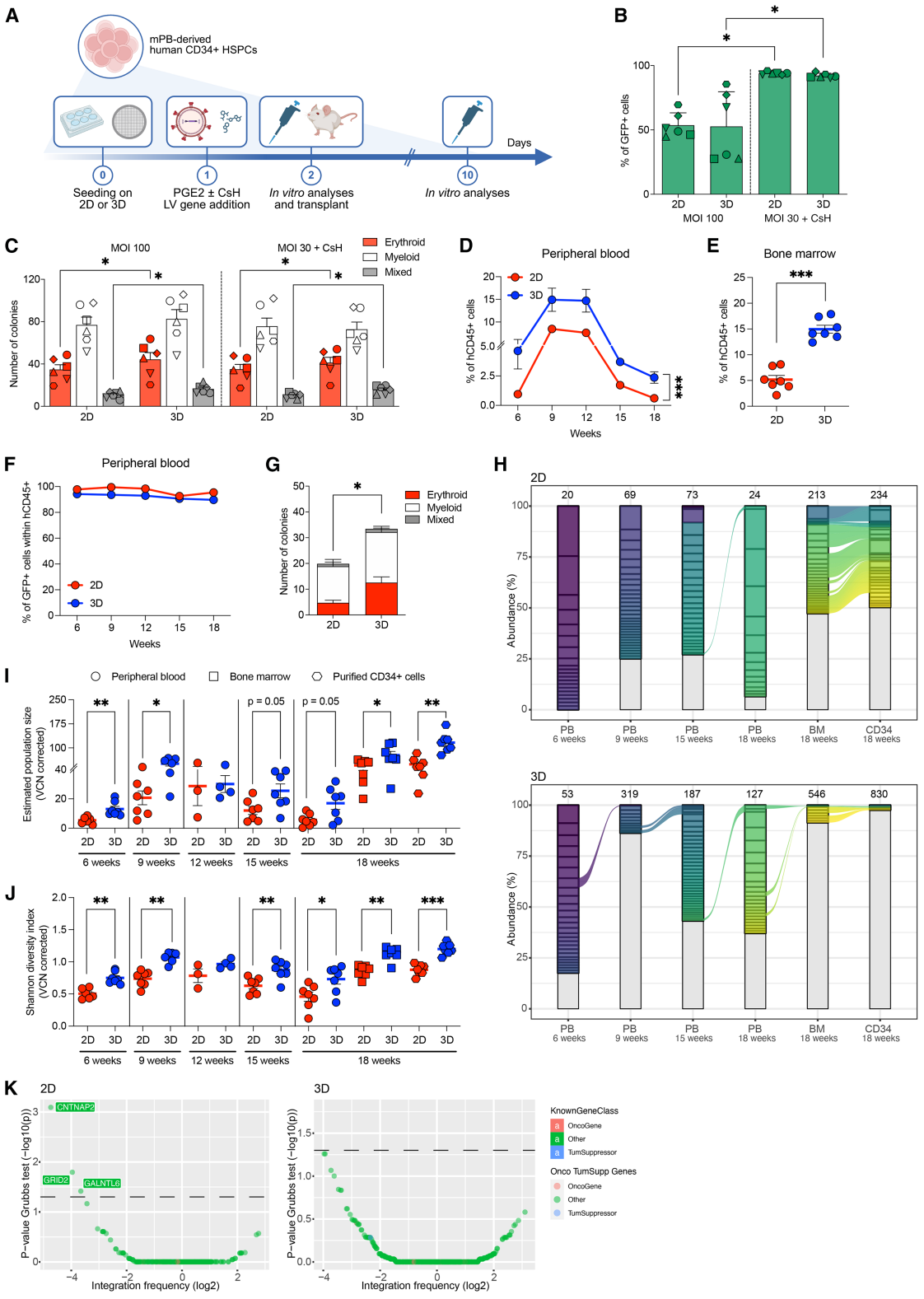

Figure 4. Nichoids improve the engraftment and clonal output of HSPCs upon gene addition

(A) Experimental workflow. Human mPB-derived HSPCs were seeded on 2D or 3D immediately after thawing and transduced on day 1 with a GFP-expressing LV vector in the presence of PGE2 alone or in combination with CsH. Specifically, transduction was performed directly on the scaffolds at MOI 100 for PGE2 alone

(legend continued on next page)

preferential enrichment of common ISs (CISs) within oncogene or tumor suppressor loci (Figures 4K and S6L).

Altogether, our data extend the beneficial properties of nichoids beyond precise GE, with 3D culture increasing the number and diversity of engrafting HSPC clones upon LV-mediated gene addition.

3D culture ameliorates the engraftment and clonal complexity of gene-corrected HSPCs in WAS

Lastly, we aimed to confirm our findings in a clinically relevant setting, specifically in a genetic disease with an already validated GT protocol. To this end, we obtained mPB-derived CD34+ cells from two Wiskott-Aldrich syndrome (WAS) patients and performed two rounds of LV transduction according to the clinical protocol,[73] transferring a functional copy of the WAS protein (WASP) using good manufacturing practice (GMP)-compliant vectors and reagents. As in clinical manufacturing, HSPCs were seeded in 2D upon coating with retronectin. Conversely, retronectin was not introduced in the 3D group to avoid interfering with cell retrieval from nichoids (Figure 5A).

While we found comparable cell viability and subset composition (Figures S7A and S7B), the VCN was lower in the nichoid group (Figure S7C). This was likely caused by the lack of retronectin, as suggested by similar transduction experiments in HSPCs from healthy donors (Figure S7D). Nevertheless, the mixed-colony output was higher in the 3D condition even in this diseased-background setting (Figure 5B).

To further corroborate these data, we then performed xenotransplantation and found improved engraftment in the PB of mice from the 3D group at the first time point (Figure 5C), suggesting that nichoid culture may facilitate an earlier hematopoietic recovery of GT-treated patients. Moreover, we observed higher human chimerism in the BM and the SP at the end of the experiment (Figures 5D and 5E), with VCN reflecting the measurement of preinfusion cells (Figure S7E). When looking at graft composition, we reported a modest increase in myeloid cells in the PB and CD34+ cells in the BM of the 3D condition, while the SP composition was comparable between groups (Figures S7F–S7H).

At last, we performed IS analyses to monitor the clonal dynamics of engrafting HSPCs and further characterize the efficacy and safety of integrating nichoids into the gene addition workflow for WAS. In line with the higher VCN, the presence of unique integrations was generally more abundant in the 2D group (Figure S7I). In addition, no clonal expansion was reported in any of the mice, with only a moderate persistence of PB-repopulating clones over time (Figures 5F and S7J). Yet, despite the different transduction efficiencies, the estimated population size of engineered cells was comparable between conditions (Figure 5G), with improved clonal diversity in the nichoid group (Figure 5H), indicating a more desirable clonal profile for therapeutic scopes. Finally, none of the mice showed preferential enrichment of CIS within oncogene or tumor suppressor loci (Figures 5I and S7K), consolidating the safety of this approach.

In summary, 3D culture enhances the repopulating capacity and clonal complexity of engineered HSPCs from WAS patients, conceivably enabling more efficient and safer clinical applications.

DISCUSSION

Despite the constant optimization of *ex vivo* culture conditions, maintaining or potentially expanding functional HSCs remains a challenge.[74] In this context, we reasoned that GT protocols could benefit from the adoption of innovative 3D systems providing mechanical support to HSCs during *ex vivo* manipulation. Consistent with the emerging concept of early-culture adaptation,[30,75] seeding HSPCs on nichoids from the very beginning of the *ex vivo* culture profoundly rewires their transcriptional profile, limiting the accumulation of DNA damage and influencing cellular metabolism, reflecting features of slow cycling and more functional stem cells.[32,53–55] Mechanistically, nichoids prevent HSPC deformation typical of 2D cultures, preserving nuclear morphology and tubulin polarity, which are closely tied with stem cell function. Indeed, squashing imposes mechanical stress on nuclei, promoting chromatin remodeling, DDR activation, and premature exhaustion,[49,76–78] and HSPCs enlarge under stress conditions, including repeated cell divisions and aging.[79] Likewise, loss of tubulin polarity caused by the upregulation of the Rho GTPase *CDC42* drives epigenetic rewiring, alterations of cell division, aging, and functional decline of HSCs.[56,80,81] Therefore, nichoids may prevent the accumulation of aging-like detrimental responses occurring in conventional 2D cultures, presumably through the sole regulation of mechanical forces.

While pharmacological modulation of individual pathways is unlikely to recapitulate the complex effects induced by 3D culture, future studies could explore dynamic cell cultures in stirred or

and MOI 30 with CsH. After 14 h from transduction (day 2), HSPCs from both the 2D and 3D conditions were collected for downstream analyses on day 2 and seeded in 2D for VCN analyses on day 10. Transplantation was performed only for the CsH condition.
(B) Percentage of GFP+ HSPCs by FACS analysis on day 10 ($n = 6$). Wilcoxon test.
(C) Number of erythroid, myeloid, and mixed colonies generated in the CFU-C assay from transduced HSPCs seeded on day 2 ($n = 6$). Wilcoxon test.
(D and E) Percentage of hCD45+ cells measured in the PB (D) over time and BM (E) at the endpoint of transplanted mice ($n = 7$). Mann-Whitney test (calculated at the last time point for PB).
(F) Percentage of GFP+ cells (within hCD45+ cells) in the PB over time from mice in (D) ($n = 7$).
(G) Number of erythroid, myeloid, and mixed colonies generated by BM-derived CD34+ cells purified from mice in (E) ($n = 7$). Mann-Whitney test.
(H) Representative plots of tracked ISs and their relative abundance over time from mice of the 2D (top, mouse A4) and 3D (bottom, mouse B12) conditions. Each colored bar univocally identifies an IS with >1% representation in at least one time point, with its abundance proportional to the height of the bar, and a colored ribbon connecting two neighboring time points for each recaptured clone. The total number of unique ISs is reported on each bar.
(I and J) Estimated clonal population size (I) and diversity measured by Shannon index (J) normalized on VCN from IS analyses. Mann-Whitney test.
(K) Representative plots of CISs from mice of the 2D (left, mouse A4) and 3D (right, mouse B12) conditions. Each dot represents a gene, labeled with the corresponding color if observed as significant. The dashed line is the alpha value 0.05. Grubbs test.
Mean ± SEM. *$p < 0.05$, **$p < 0.01$, ***$p < 0.001$.
See also Figure S6 and Tables S1 and S3.

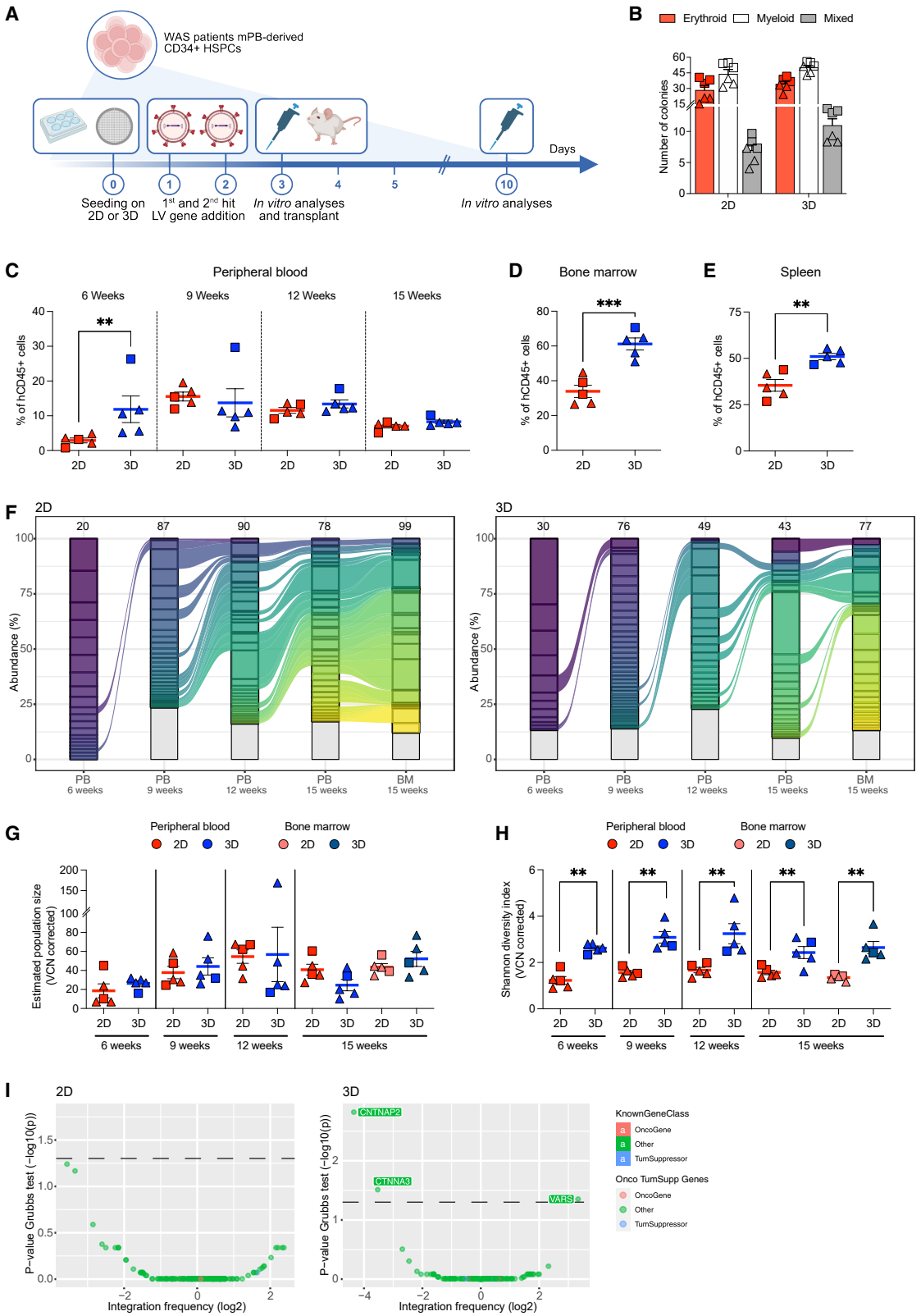

Figure 5. Nichoids improve the engraftment and clonal complexity of gene-corrected HSPCs in WAS

(A) Experimental workflow. mPB-derived HSPCs from WAS patients were seeded on 2D (upon coating with retronectin) or 3D (without retronectin coating) immediately after thawing and transduced directly on the scaffolds with two hits of WASP-expressing LV on days 1 and 2 at MOI 100. After 14 h from the second

(legend continued on next page)

perfused bioreactors,[82,83] which could further modulate cell mechanobiology. Besides, nichoids should be compared with other 3D systems developed for human HSPCs but not yet tested for genetic engineering.[84–88] For instance, hydrogels and bioprinting offer a customizable solution to mimic the biochemical properties of the ECM and generate more complex 3D structures using biomaterials and living cells, providing tunable architectures that can be functionalized with bioactive molecules. Conversely, nichoids are nanoengineered through two-photon polymerization, which enables higher spatial resolution compared with traditional bioprinting techniques,[89] and lack ECM functionalization to avoid introducing potential degradable molecules, as well as facilitating cell retrieval from the scaffold, which represents one of the critical limitations of current 3D approaches. Given the multitude of fabrication techniques and customizable parameters, such as stiffness, porosity, and biochemical cues, rapid advances in the field may allow future side-by-side comparisons to identify optimal 3D conditions that faithfully recapitulate the physiological HSC microenvironment, further improving HSPC-based therapies.

Beyond HSPC biology, our work shows that nichoids support efficient genetic engineering across multiple GT settings, including Cas9/AAV6-, BE-, and PE-mediated GE and LV-mediated gene addition. Most importantly, 3D culture enhances the engraftment and clonal output of edited cells, potentially improving efficacy and safety by diminishing the risk of clonal hematopoiesis and malignant transformation in patients.[3,22,33,34,90] Additionally, we found a broad modulation of DNA damage, DDR signaling, and DNA repair pathways in 3D, with no insertional mutagenesis and pre-malignant clonal expansion. Whether nichoids affect other genotoxic events related to genetic engineering, such as on/off-targets, indels, and chromosomal rearrangements, remains to be elucidated.[26,91–93] However, our results suggest that 3D culture may improve genome integrity by limiting culture-associated DNA damage, endowing engineered HSPCs with enhanced safety profiles.

Finally, while we validated our findings in WAS, we anticipate that 3D culture could particularly benefit BM-failure conditions, like Dyskeratosis Congenita and Fanconi anemia, in which HSPCs are progressively lost during *ex vivo* manipulation.[94,95] In addition, 3D culture may also enhance HSPC expansion protocols for allogeneic transplantation.[74,96,97] Besides, future studies may further compare our approach with alternative therapeutic strategies, such as *in vivo* delivery of editing reagents or cells directly embedded in 3D matrices.[88,98] However, while conceptually exciting, *in vivo* GT for HSPCs is still in its early stages and currently faces several technical and safety challenges, such as delivery modalities, limited targeting efficiency, off-target activity, and difficulties in controlling dose and biodistribution. Similarly, translation of implantable 3D scaffolds carrying engineered cells would require careful evaluation of several key aspects, including achieving efficient genetic engineering either outside the scaffold or directly *in situ*, ensuring that implantation does not inadvertently transfer residual reagents and viral particles into the patient, and verifying long-term stability and biocompatibility post-implant.

In conclusion, our work establishes 3D culture as an innovative strategy to preserve the functionality of HSCs during *ex vivo* manipulation for multiple clinical scopes, laying the foundation for enabling more effective and safer gene and cell therapies.

Limitations of the study

Here, we demonstrated the potential of 3D culture in small-scale preclinical testing across multiple relevant contexts. However, direct *in vivo* validation of every possible combination of HSPC source and genetic engineering strategy will be necessary to confirm these findings within each specific application. Additionally, our xenotransplantation experiments were performed by injection of matching numbers of HSPCs, although different settings, including limiting-dilution and injection of the total outgrowths of the same starting HSPC number (t_0 equivalent), would allow further dissection of the biological benefits of 3D culture and technical differences related to cell recovery from the scaffolds. Finally, nichoids will require additional refinements and optimization to support production scale-up and incorporation into GMP-compliant systems for clinical applications. Specifically, large-scale production would require *ad hoc* investments to speed up manufacturing and meet clinical demands. Moreover, the current design of nichoids, fabricated on a glass support, may limit their immediate integration into cell expansion bags usually employed in clinical workflows. However, we envision that nichoids could fit inside custom-designed bioreactors, which may also further facilitate cell retrieval.

RESOURCE AVAILABILITY

Lead contact

Further information and requests should be directed to and will be fulfilled by Raffaella Di Micco (dimicco.raffaella@hsr.it).

Materials availability

This study did not generate new reagents. Nichoids can be obtained through collaboration with Manuela Teresa Raimondi (manuela.raimondi@polimi.it) or purchased from MOAB S.R.L. (https://moab-research.com/).

round of transduction (day 3), HSPCs from both the 2D and 3D conditions were collected for downstream analyses on day 3 and seeded in 2D for VCN analyses on day 10. Three independent technical replicates were performed for each donor (different symbols identify the two WAS patients).

(B) Number of erythroid, myeloid, and mixed colonies generated in the CFU-C assay from transduced HSPCs seeded on day 3 ($n = 6$).

(C–E) Percentage of hCD45+ cells measured in the PB (C) over time and in the BM (D) and SP (E) at the endpoint ($n = 5$). Random-intercept linear mixed-effects (LME) model.

(F) Representative plots of tracked ISs and their relative abundance over time from mice of the 2D (left, mouse A4) and 3D (right, mouse B6) conditions. Each colored bar univocally identifies an IS with >1% representation in at least one time point, with its abundance proportional to the height of the bar, and a colored ribbon connecting two neighboring time points for each recaptured clone. The total number of unique ISs is reported on each bar.

(G and H) Estimated clonal population size (G) and diversity measured by Shannon index (H) normalized on VCN from IS analyses. Random-intercept LME model.

(I) Representative plots of CISs from mice of the 2D (left, mouse A4) and 3D (right, mouse B6) conditions. Each dot represents a gene, labeled with the corresponding color if observed as significant. The dashed line is the alpha value 0.05. Grubbs test.

Mean ± SEM. $^{**}p < 0.01$, $^{***}p < 0.001$.

See also Figure S7 and Tables S1 and S3.

Data and code availability

- Data used for transcriptomic and IS analyses are accessible at the following repositories:https://www.ncbi.nlm.nih.gov/geo/query/acc.cgi?acc=GSE280536 and https://github.com/calabrialab/Code_3D_Scaffold.
- Codes used for the generation of results are accessible at the following repositories: http://www.bioinfotiget.it/gitlab/custom/Midena2024 and https://github.com/calabrialab/Code_3D_Scaffold.

ACKNOWLEDGMENTS

The authors would like to thank the FRACTAL and ALEMBIC facilities at San Raffaele Hospital, especially Valeria Berno for Arivis Vision4D analyses. Illustrations were created with BioRender.com. F.M., L.A., and R.V. conducted this study, partially fulfilling their Ph.D. in Molecular Medicine, Vita-Salute San Raffaele University. F.G. conducted this study, partially fulfilling his Ph.D. in Information Technology, Politecnico di Milano. G.F. conducted this study, partially fulfilling his Ph.D. in Translational and Molecular Medicine, University of Milano Bicocca. Work in the R.D.M., L.N., and B.G. lab was supported by the Horizon Europe 2020 Program X-PAND grant (G.A. 101070950). Work in the R.D.M. laboratory was supported by a Career Development Award from the Human Frontier Science Program, the New York Stem Cell Foundation, My First AIRC Grant (MFAG 2019–PI ID.23321), the European Research Council (consolidator grant 101003186, ReviveSTEM), and Fondazione Telethon (SR-Tiget Core Grant, Tele21-E5). R.D.M. is a New York Stem Cell Foundation Robertson Investigator.

AUTHOR CONTRIBUTIONS

F.M. planned and performed experiments and analyzed and interpreted the data; L.A. performed and analyzed experiments; C.C. and L.C. produced nichoids, and E.J. performed immunofluorescence analyses on them, supervised by M.T.R., G.C., and R.O.; M.B., F.G., and T.T. performed bioinformatics analysis and interpreted computational data, supervised by I.M. and E.M.; E.C. and K.G. provided help with animal experiments; F.B. and S.A. performed VCN and IS analyses, supervised by E.M.; R.V. performed comet assay and helped with several experiments; L.d.V. performed proliferation analyses over time and discussed the data; D.B. and M.F. helped setting up alternative 3D cultures and performed immunofluorescence analyses on them, supervised by C.S. and A.B.; E.Z. helped with LV experiments, supervised by B.G. and M.R.; F. Ferrua. and F. Fraschetta. provided samples from WAS patients, supervised by A.A.; G.F. performed initial experiments on 3D culture; C.B. and F.C. supervised and performed statistical analyses; M.F. helped with editing experiments, supervised by S.F. and L.N.; S.F., B.G., C.S., A.B., L.N., A.A., E.M., and M.T.R. provided intellectual input and critical discussion. R.D.M. conceived the study, coordinated and interpreted the data, secured funding, and supervised the research. F.M. and R.D.M. wrote the manuscript with inputs from all the authors.

DECLARATION OF INTERESTS

F.M., L.d.V., S.F., L.N., and R.D.M. are inventors of patents on applications of GE in HSPCs owned and managed by the San Raffaele Scientific Institute and the Telethon Foundation. M.T.R., G.C., and R.O. are inventors of patents on the nichoid culture substrate and co-founders and quota holders of MOAB S.R.L.

STAR★METHODS

Detailed methods are provided in the online version of this paper and include the following:

SUPPLEMENTAL INFORMATION

Supplemental information can be found online at https://doi.org/10.1016/j.stem.2025.12.016.

Received: June 18, 2025
Revised: November 5, 2025
Accepted: December 15, 2025
Published: January 8, 2026

REFERENCES

1. Naldini, L. (2015). Gene therapy returns to centre stage. Nature *526*, 351–360. https://doi.org/10.1038/nature15818.
2. Ferrari, G., Thrasher, A.J., and Aiuti, A. (2021). Gene therapy using haematopoietic stem and progenitor cells. Nat. Rev. Genet. *22*, 216–234. https://doi.org/10.1038/s41576-020-00298-5.
3. Ferrari, S., Valeri, E., Conti, A., Scala, S., Aprile, A., Di Micco, R., Kajaste-Rudnitski, A., Montini, E., Ferrari, G., Aiuti, A., et al. (2023). Genetic engineering meets hematopoietic stem cell biology for next-generation gene therapy. Cell Stem Cell *30*, 549–570. https://doi.org/10.1016/j.stem.2023.04.014.
4. Morgan, R.A., Gray, D., Lomova, A., and Kohn, D.B. (2017). Hematopoietic Stem Cell Gene Therapy: Progress and Lessons Learned. Cell Stem Cell *21*, 574–590. https://doi.org/10.1016/j.stem.2017.10.010.
5. Cavazzana-Calvo, M., Hacein-Bey, S., De Saint Basile, G., Gross, F., Yvon, E., Nusbaum, P., Selz, F., Hue, C., Certain, S., Casanova, J.L., et al. (2000). Gene therapy of human severe combined immunodeficiency (SCID)-X1 disease. Science *288*, 669–672. https://doi.org/10.1126/science.288.5466.669.
6. Aiuti, A., Slavin, S., Aker, M., Ficara, F., Deola, S., Mortellaro, A., Morecki, S., Andolfi, G., Tabucchi, A., Carlucci, F., et al. (2002). Correction of ADA-SCID by stem cell gene therapy combined with nonmyeloablative conditioning. Science *296*, 2410–2413. https://doi.org/10.1126/science.1070104.
7. Aiuti, A., Biasco, L., Scaramuzza, S., Ferrua, F., Cicalese, M.P., Baricordi, C., Dionisio, F., Calabria, A., Giannelli, S., Castiello, M.C., et al. (2013). Lentiviral Hematopoietic Stem Cell Gene Therapy in Patients with Wiskott-Aldrich Syndrome. Science *341*, 1233151. https://doi.org/10.1126/science.1233151.
8. Biffi, A., Montini, E., Lorioli, L., Cesani, M., Fumagalli, F., Plati, T., Baldoli, C., Martino, S., Calabria, A., Canale, S., et al. (2013). Lentiviral hematopoietic stem cell gene therapy benefits metachromatic leukodystrophy. Science *341*, 1233158. https://doi.org/10.1126/science.1233158.
9. Schiroli, G., Ferrari, S., Conway, A., Jacob, A., Capo, V., Albano, L., Plati, T., Castiello, M.C., Sanvito, F., Gennery, A.R., et al. (2017). Preclinical modeling highlights the therapeutic potential of hematopoietic stem cell gene editing for correction of SCID-X1. Sci. Transl. Med. *9*, eaan0820. https://doi.org/10.1126/scitranslmed.aan0820.
10. Zeng, J., Wu, Y., Ren, C., Bonanno, J., Shen, A.H., Shea, D., Gehrke, J.M., Clement, K., Luk, K., Yao, Q., et al. (2020). Therapeutic base editing of human hematopoietic stem cells. Nat. Med. *26*, 535–541. https://doi.org/10.1038/S41591-020-0790-Y.
11. Everette, K.A., Newby, G.A., Levine, R.M., Mayberry, K., Jang, Y., Mayuranathan, T., Nimmagadda, N., Dempsey, E., Li, Y., Bhoopalan,

S.V., et al. (2023). Ex vivo prime editing of patient haematopoietic stem cells rescues sickle-cell disease phenotypes after engraftment in mice. Nat. Biomed. Eng. *7*, 616–628. https://doi.org/10.1038/s41551-023-01026-0.

12. Calabria, A., Spinozzi, G., Cesana, D., Buscaroli, E., Benedicenti, F., Pais, G., Gazzo, F., Scala, S., Lidonnici, M.R., Scaramuzza, S., et al. (2024). Long-term lineage commitment in haematopoietic stem cell gene therapy. Nature *636*, 162–171. https://doi.org/10.1038/s41586-024-08250-x.
13. Kohn, D.B., Booth, C., Shaw, K.L., Xu-Bayford, J., Garabedian, E., Trevisan, V., Carbonaro-Sarracino, D.A., Soni, K., Terrazas, D., Snell, K., et al. (2021). Autologous Ex Vivo Lentiviral Gene Therapy for Adenosine Deaminase Deficiency. N. Engl. J. Med. *384*, 2002–2013. https://doi.org/10.1056/NEJMoa2027675.
14. Kuo, C.Y., and Kohn, D.B. (2020). Overview of the current status of gene therapy for primary immune deficiencies (PIDs). J. Allergy Clin. Immunol. *146*, 229–233. https://doi.org/10.1016/J.JACI.2020.05.024.
15. Gentner, B., Tucci, F., Galimberti, S., Fumagalli, F., De Pellegrin, M., Silvani, P., Camesasca, C., Pontesilli, S., Darin, S., Ciotti, F., et al. (2021). Hematopoietic Stem- and Progenitor-Cell Gene Therapy for Hurler Syndrome. N. Engl. J. Med. *385*, 1929–1940. https://doi.org/10.1056/NEJMoa2106596.
16. Marktel, S., Scaramuzza, S., Cicalese, M.P., Giglio, F., Galimberti, S., Lidonnici, M.R., Calbi, V., Assanelli, A., Bernardo, M.E., Rossi, C., et al. (2019). Intrabone hematopoietic stem cell gene therapy for adult and pediatric patients affected by transfusion-dependent ß-thalassemia. Nat. Med. *25*, 234–241. https://doi.org/10.1038/s41591-018-0301-6.
17. Esrick, E.B., Lehmann, L.E., Biffi, A., Achebe, M., Brendel, C., Ciuculescu, M.F., Daley, H., MacKinnon, B., Morris, E., Federico, A., et al. (2021). Post-Transcriptional Genetic Silencing of BCL11A to Treat Sickle Cell Disease. N. Engl. J. Med. *384*, 205–215. https://doi.org/10.1056/NEJMoa2029392.
18. Río, P., Navarro, S., Wang, W., Sánchez-Domínguez, R., Pujol, R.M., Segovia, J.C., Bogliolo, M., Merino, E., Wu, N., Salgado, R., et al. (2019). Successful engraftment of gene-corrected hematopoietic stem cells in non-conditioned patients with Fanconi anemia. Nat. Med. *25*, 1396–1401. https://doi.org/10.1038/s41591-019-0550-z.
19. Frangoul, H., Altshuler, D., Cappellini, M.D., Chen, Y.-S., Domm, J., Eustace, B.K., Foell, J., de la Fuente, J., Grupp, S., Handgretinger, R., et al. (2021). CRISPR-Cas9 Gene Editing for Sickle Cell Disease and β--Thalassemia. N. Engl. J. Med. *384*, 252–260. https://doi.org/10.1056/NEJMOA2031054.
20. Witkowsky, L., Norstad, M., Glynn, A.R., and Kliegman, M. (2023). Towards affordable CRISPR genomic therapies: a task force convened by the Innovative Genomics Institute. Gene Ther. *30*, 747–752. https://doi.org/10.1038/s41434-023-00392-3.
21. Aiuti, A., Pasinelli, F., and Naldini, L. (2022). Ensuring a future for gene therapy for rare diseases. Nat. Med. *28*, 1985–1988. https://doi.org/10.1038/s41591-022-01934-9.
22. Tucci, F., Scaramuzza, S., Aiuti, A., and Mortellaro, A. (2021). Update on Clinical Ex Vivo Hematopoietic Stem Cell Gene Therapy for Inherited Monogenic Diseases. Mol. Ther. *29*, 489–504. https://doi.org/10.1016/J.YMTHE.2020.11.020.
23. Piras, F., Riba, M., Petrillo, C., Lazarevic, D., Cuccovillo, I., Bartolaccini, S., Stupka, E., Gentner, B., Cittaro, D., Naldini, L., et al. (2017). Lentiviral vectors escape innate sensing but trigger p53 in human hematopoietic stem and progenitor cells. EMBO Mol. Med. *9*, 1198–1211. https://doi.org/10.15252/emmm.201707922.
24. Schiroli, G., Conti, A., Ferrari, S., Della Volpe, L., Jacob, A., Albano, L., Beretta, S., Calabria, A., Vavassori, V., Gasparini, P., et al. (2019). Precise Gene Editing Preserves Hematopoietic Stem Cell Function following Transient p53-Mediated DNA Damage Response. Cell Stem Cell *24*, 551–565.e8. https://doi.org/10.1016/j.stem.2019.02.019.
25. Fiumara, M., Ferrari, S., Omer-Javed, A., Beretta, S., Albano, L., Canarutto, D., Varesi, A., Gaddoni, C., Brombin, C., Cugnata, F., et al. (2023). Genotoxic effects of base and prime editing in human hematopoietic stem cells. Nat. Biotechnol. *42*, 877–891. https://doi.org/10.1038/s41587-023-01915-4.
26. Leibowitz, M.L., Papathanasiou, S., Doerfler, P.A., Blaine, L.J., Sun, L., Yao, Y., Zhang, C.Z., Weiss, M.J., and Pellman, D. (2021). Chromothripsis as an on-target consequence of CRISPR–Cas9 genome editing. Nat. Genet. *53*, 895–905. https://doi.org/10.1038/s41588-021-00838-7.
27. Cesana, D., Cicalese, M.P., Calabria, A., Merli, P., Caruso, R., Volpin, M., Rudilosso, L., Migliavacca, M., Barzaghi, F., Fossati, C., et al. (2024). A case of T-cell acute lymphoblastic leukemia in retroviral gene therapy for ADA-SCID. Nat. Commun. *15*, 3662. https://doi.org/10.1038/S41467-024-47866-5.
28. Conti, A., Giannetti, K., Midena, F., Beretta, S., Gualandi, N., De Marco, R., Carsana, E., Varesi, A., Tavella, T., Alessandrini, L., et al. (2025). Senescence and inflammation are unintended adverse consequences of CRISPR-Cas9/AAV6-mediated gene editing in hematopoietic stem cells. Cell Rep. Med. *6*, 102157. https://doi.org/10.1016/J.XCRM.2025.102157.
29. Glimm, H., Oh, I.H., and Eaves, C.J. (2000). Human hematopoietic stem cells stimulated to proliferate in vitro lose engraftment potential during their S/G(2)/M transit and do not reenter G(0). Blood *96*, 4185–4193. https://doi.org/10.1182/blood.v96.13.4185.
30. Johnson, C.S., Williams, M., Sham, K., Belluschi, S., Ma, W., Wang, X., Lau, W.W.Y., Kaufmann, K.B., Krivdova, G., Calderbank, E.F., et al. (2024). Adaptation to ex vivo culture reduces human hematopoietic stem cell activity independently of the cell cycle. Blood *144*, 729–741. https://doi.org/10.1182/BLOOD.2023021426.
31. Della Volpe, L., Lee, A.J., Antoszewski, M., Deik, A.A., Safina, K.R., Gao, T., Guo, C.J., Ye, T., Lyu, P., Martin-Rufino, J.D., et al. (2025). Inhibiting ferroptosis enhances ex vivo expansion of human haematopoietic stem cells. Nat. Cell Biol. 1–11. https://doi.org/10.1038/s41556-025-01814-7.
32. Della Volpe, L., Midena, F., Vacca, R., Tavella, T., Alessandrini, L., Farina, G., Brandas, C., Lo Furno, E.L., Giannetti, K., Carsana, E., et al. (2024). A p38 MAPK-ROS axis fuels proliferation stress and DNA damage during CRISPR-Cas9 gene editing in hematopoietic stem and progenitor cells. Cell Rep. Med. *5*, 101823. https://doi.org/10.1016/J.XCRM.2024.101823.
33. Masiuk, K.E., Brown, D., Laborada, J., Hollis, R.P., Urbinati, F., and Kohn, D.B. (2017). Improving Gene Therapy Efficiency through the Enrichment of Human Hematopoietic Stem Cells. Mol. Ther. *25*, 2163–2175. https://doi.org/10.1016/J.YMTHE.2017.05.023.
34. Ferrari, S., Jacob, A., Beretta, S., Unali, G., Albano, L., Vavassori, V., Cittaro, D., Lazarevic, D., Brombin, C., Cugnata, F., et al. (2020). Efficient gene editing of human long-term hematopoietic stem cells validated by clonal tracking. Nat. Biotechnol. *38*, 1298–1308. https://doi.org/10.1038/s41587-020-0551-y.
35. Petrillo, C., Thorne, L.G., Unali, G., Schiroli, G., Giordano, A.M.S., Piras, F., Cuccovillo, I., Petit, S.J., Ahsan, F., Noursadeghi, M., et al. (2018). Cyclosporine H Overcomes Innate Immune Restrictions to Improve Lentiviral Transduction and Gene Editing In Human Hematopoietic Stem Cells. Cell Stem Cell *23*, 820–832.e9. https://doi.org/10.1016/j.stem.2018.10.008.
36. Baik, R., Cromer, M.K., Glenn, S.E., Vakulskas, C.A., Chmielewski, K.O., Dudek, A.M., Feist, W.N., Klermund, J., Shipp, S., Cathomen, T., et al. (2024). Transient inhibition of 53BP1 increases the frequency of targeted integration in human hematopoietic stem and progenitor cells. Nat. Commun. *15*, 111. https://doi.org/10.1038/s41467-023-43413-w.
37. Zonari, E., Desantis, G., Petrillo, C., Boccalatte, F.E., Lidonnici, M.R., Kajaste-Rudnitski, A., Aiuti, A., Ferrari, G., Naldini, L., and Gentner, B. (2017). Efficient Ex Vivo Engineering and Expansion of Highly Purified Human Hematopoietic Stem and Progenitor Cell Populations for Gene Therapy. Stem Cell Rep. *8*, 977–990. https://doi.org/10.1016/j.stemcr.2017.02.010.
38. Rai, R., Naseem, A., Vetharoy, W., Steinberg, Z., Thrasher, A.J., Santilli, G., and Cavazza, A. (2023). An improved medium formulation for efficient ex vivo gene editing, expansion and engraftment of hematopoietic stem

and progenitor cells. Mol. Ther. Methods Clin. Dev. *29*, 58–69. https://doi.org/10.1016/J.OMTM.2023.02.014.

39. Horwitz, M.E., Chao, N.J., Rizzieri, D.A., Long, G.D., Sullivan, K.M., Gasparetto, C., Chute, J.P., Morris, A., McDonald, C., Waters-Pick, B., et al. (2014). Umbilical cord blood expansion with nicotinamide provides long-term multilineage engraftment. J. Clin. Investig. *124*, 3121–3128. https://doi.org/10.1172/JCI74556.
40. Fares, I., Chagraoui, J., Gareau, Y., Gingras, S., Ruel, R., Mayotte, N., Csaszar, E., Knapp, D.J.H.F., Miller, P., Ngom, M., et al. (2014). Cord blood expansion. Pyrimidoindole derivatives are agonists of human hematopoietic stem cell self-renewal. Science *345*, 1509–1512. https://doi.org/10.1126/science.1256337.
41. Sakurai, M., Ishitsuka, K., Ito, R., Wilkinson, A.C., Kimura, T., Mizutani, E., Nishikii, H., Sudo, K., Becker, H.J., Takemoto, H., et al. (2023). Chemically defined cytokine-free expansion of human haematopoietic stem cells. Nature *615*, 127–133. https://doi.org/10.1038/s41586-023-05739-9.
42. Becker, H.J., Ishida, R., Wilkinson, A.C., Kimura, T., Lee, M.S.J., Coban, C., Ota, Y., Tanaka, Y., Roskamp, M., Sano, T., et al. (2023). Controlling genetic heterogeneity in gene-edited hematopoietic stem cells by single-cell expansion. Cell Stem Cell *30*, 987–1000.e8. https://doi.org/10.1016/J.STEM.2023.06.002.
43. Lundin, V., Sugden, W.W., Theodore, L.N., Sousa, P.M., Han, A., Chou, S., Wrighton, P.J., Cox, A.G., Ingber, D.E., Goessling, W., et al. (2020). YAP Regulates Hematopoietic Stem Cell Formation in Response to the Biomechanical Forces of Blood Flow. Dev. Cell *52*, 446–460.e5. https://doi.org/10.1016/J.DEVCEL.2020.01.006.
44. Adamo, L., Naveiras, O., Wenzel, P.L., McKinney-Freeman, S., Mack, P.J., Gracia-Sancho, J., Suchy-Dicey, A., Yoshimoto, M., Lensch, M.W., Yoder, M.C., et al. (2009). Biomechanical forces promote embryonic haematopoiesis. Nature *459*, 1131–1135. https://doi.org/10.1038/nature08073.
45. Holst, J., Watson, S., Lord, M.S., Eamegdool, S.S., Bax, D.V., Nivison-Smith, L.B., Kondyurin, A., Ma, L., Oberhauser, A.F., Weiss, A.S., et al. (2010). Substrate elasticity provides mechanical signals for the expansion of hemopoietic stem and progenitor cells. Nat. Biotechnol. *28*, 1123–1128. https://doi.org/10.1038/nbt.1687.
46. Altrock, E., Muth, C.A., Klein, G., Spatz, J.P., and Lee-Thedieck, C. (2012). The significance of integrin ligand nanopatterning on lipid raft clustering in hematopoietic stem cells. Biomaterials *33*, 3107–3118. https://doi.org/10.1016/J.BIOMATERIALS.2012.01.002.
47. Zhang, P., Zhang, C., Li, J., Han, J., Liu, X., and Yang, H. (2019). The physical microenvironment of hematopoietic stem cells and its emerging roles in engineering applications. Stem Cell Res. Ther. *10*, 327. https://doi.org/10.1186/S13287-019-1422-7.
48. Ni, F., Yu, W.M., Wang, X., Fay, M.E., Young, K.M., Qiu, Y., Lam, W.A., Sulchek, T.A., Cheng, T., Scadden, D.T., et al. (2019). Ptpn21 Controls Hematopoietic Stem Cell Homeostasis and Biomechanics. Cell Stem Cell *24*, 608–620.e6. https://doi.org/10.1016/J.STEM.2019.02.009.
49. Li, H., Luo, Q., Shan, W., Cai, S., Tie, R., Xu, Y., Lin, Y., Qian, P., and Huang, H. (2021). Biomechanical cues as master regulators of hematopoietic stem cell fate. Cell. Mol. Life Sci. *78*, 5881–5902. https://doi.org/10.1007/S00018-021-03882-Y.
50. Nava, M.M., Piuma, A., Figliuzzi, M., Cattaneo, I., Bonandrini, B., Zandrini, T., Cerullo, G., Osellame, R., Remuzzi, A., and Raimondi, M.T. (2016). Two-photon polymerized "nichoid" substrates maintain function of pluripotent stem cells when expanded under feeder-free conditions. Stem Cell Res. Ther. *7*, 132. https://doi.org/10.1186/s13287-016-0387-z.
51. Miller, C.L., and Lai, B. (2005). Human and mouse hematopoietic colony-forming cell assays. Methods Mol. Biol. *290*, 71–89. https://doi.org/10.1385/1-59259-838-2:071.
52. Belluschi, S., Calderbank, E.F., Ciaurro, V., Pijuan-Sala, B., Santoro, A., Mende, N., Diamanti, E., Sham, K.Y.C., Wang, X., Lau, W.W.Y., et al. (2018). Myelo-lymphoid lineage restriction occurs in the human haematopoietic stem cell compartment before lymphoid-primed multipotent progenitors. Nat. Commun. *9*, 4100. https://doi.org/10.1038/s41467-018-06442-4.
53. García-Prat, L., Kaufmann, K.B., Schneiter, F., Voisin, V., Murison, A., Chen, J., Chan-Seng-Yue, M., Gan, O.I., McLeod, J.L., Smith, S.A., et al. (2021). TFEB-mediated endolysosomal activity controls human hematopoietic stem cell fate. Cell Stem Cell *28*, 1838–1850.e10. https://doi.org/10.1016/J.STEM.2021.07.003.
54. Lauridsen, F.K.B., Jensen, T.L., Rapin, N., Aslan, D., Wilhelmson, A.S., Pundhir, S., Rehn, M., Paul, F., Giladi, A., Hasemann, M.S., et al. (2018). Differences in Cell Cycle Status Underlie Transcriptional Heterogeneity in the HSC Compartment. Cell Rep. *24*, 766–780. https://doi.org/10.1016/J.CELREP.2018.06.057.
55. Cabezas-Wallscheid, N., Klimmeck, D., Hansson, J., Lipka, D.B., Reyes, A., Wang, Q., Weichenhan, D., Lier, A., Von Paleske, L., Renders, S., et al. (2014). Identification of regulatory networks in HSCs and their immediate progeny via integrated proteome, transcriptome, and DNA methylome analysis. Cell Stem Cell *15*, 507–522. https://doi.org/10.1016/J.STEM.2014.07.005.
56. Florian, M.C., Dörr, K., Niebel, A., Daria, D., Schrezenmeier, H., Rojewski, M., Filippi, M.D., Hasenberg, A., Gunzer, M., Scharffetter-Kochanek, K., et al. (2012). Cdc42 activity regulates hematopoietic stem cell aging and rejuvenation. Cell Stem Cell *10*, 520–530. https://doi.org/10.1016/J.STEM.2012.04.007.
57. Pajcini, K.V., Speck, N.A., and Pear, W.S. (2011). Notch signaling in mammalian hematopoietic stem cells. Leukemia *25*, 1525–1532. https://doi.org/10.1038/LEU.2011.127.
58. Araki, D., Fu, J.F., Huntsman, H., Cordes, S., Seifuddin, F., Alvarado, L.J., Cheruku, P.S., Cash, A., Traba, J., Li, Y., et al. (2021). NOTCH-mediated ex vivo expansion of human hematopoietic stem and progenitor cells by culture under hypoxia. Stem Cell Rep. *16*, 2336–2350. https://doi.org/10.1016/J.STEMCR.2021.08.001.
59. Butler, J.M., Nolan, D.J., Vertes, E.L., Varnum-Finney, B., Kobayashi, H., Hooper, A.T., Seandel, M., Shido, K., White, I.A., Kobayashi, M., et al. (2010). Endothelial cells are essential for the self-renewal and repopulation of Notch-dependent hematopoietic stem cells. Cell Stem Cell *6*, 251–264. https://doi.org/10.1016/J.STEM.2010.02.001.
60. Lehnertz, B., Chagraoui, J., MacRae, T., Tomellini, E., Corneau, S., Mayotte, N., Boivin, I., Durand, A., Gracias, D., and Sauvageau, G. (2021). HLF expression defines the human hematopoietic stem cell state. Blood *138*, 2642–2654. https://doi.org/10.1182/BLOOD.2021010745.
61. Liang, R., Arif, T., Kalmykova, S., Kasianov, A., Lin, M., Menon, V., Qiu, J., Bernitz, J.M., Moore, K., Lin, F., et al. (2020). Restraining Lysosomal Activity Preserves Hematopoietic Stem Cell Quiescence and Potency. Cell Stem Cell *26*, 359–376.e7. https://doi.org/10.1016/J.STEM.2020.01.013.
62. Chabi, S., Uzan, B., Naguibneva, I., Rucci, J., Fahy, L., Calvo, J., Arcangeli, M.L., Mazurier, F., Pflumio, F., and Haddad, R. (2019). Hypoxia Regulates Lymphoid Development of Human Hematopoietic Progenitors. Cell Rep. *29*, 2307–2320.e6. https://doi.org/10.1016/J.CELREP.2019.10.050.
63. Miyamoto, K., Araki, K.Y., Naka, K., Arai, F., Takubo, K., Yamazaki, S., Matsuoka, S., Miyamoto, T., Ito, K., Ohmura, M., et al. (2007). Foxo3a is essential for maintenance of the hematopoietic stem cell pool. Cell Stem Cell *1*, 101–112. https://doi.org/10.1016/J.STEM.2007.02.001.
64. Tothova, Z., Kollipara, R., Huntly, B.J., Lee, B.H., Castrillon, D.H., Cullen, D.E., McDowell, E.P., Lazo-Kallanian, S., Williams, I.R., Sears, C., et al. (2007). FoxOs are critical mediators of hematopoietic stem cell resistance to physiologic oxidative stress. Cell *128*, 325–339. https://doi.org/10.1016/J.CELL.2007.01.003.
65. Kim, K.M., Mura-Meszaros, A., Tollot, M., Krishnan, M.S., Gründl, M., Neubert, L., Groth, M., Rodriguez-Fraticelli, A., Svendsen, A.F., Campaner, S., et al. (2022). Taz protects hematopoietic stem cells from an aging-dependent decrease in PU.1 activity. Nat. Commun. *13*, 5187. https://doi.org/10.1038/S41467-022-32970-1.

66. Staal, F.J.T., Chhatta, A., and Mikkers, H. (2016). Caught in a Wnt storm: Complexities of Wnt signaling in hematopoiesis. Exp. Hematol. *44*, 451–457. https://doi.org/10.1016/J.EXPHEM.2016.03.004.

67. Famili, F., Naber, B.A.E., Vloemans, S., De Haas, E.F.E., Tiemessen, M.M., and Staal, F.J.T. (2015). Discrete roles of canonical and non-canonical Wnt signaling in hematopoiesis and lymphopoiesis. Cell Death Dis. *6*, e1981. https://doi.org/10.1038/cddis.2015.326.

68. Sulli, G., Di Micco, R., and d'Adda di Fagagna, F.D.A. (2012). Crosstalk between chromatin state and DNA damage response in cellular senescence and cancer. Nat. Rev. Cancer *12*, 709–720. https://doi.org/10.1038/nrc3344.

69. Lenti, E., Visentin, E., Bojnik, E., Neroni, A., Franchino, M., Talarico, D., Sacchetti, N., Scarfò, L., Maurizio, A., Garcia-Manteiga, J.M., et al. (2025). A spheroid model that recapitulates the protective role of the lymph node microenvironment and serves as a platform for drug testing in chronic lymphocytic leukemia. Hemasphere *9*, e70170. https://doi.org/10.1002/HEM3.70170.

70. Barozzi, D., Scagnoli, F., Barbaglio, F., Belloni, D., Ribezzi, D., Farè, S., Berno, V., Pinos, R., Sampietro, M., Pauri, M., et al. (2025). Dynamic stimulation promotes functional tissue-like organization of a 3D human lymphoid microenvironment model in vitro. Cell Rep. Methods *5*, 101105. https://doi.org/10.1016/J.CRMETH.2025.101105.

71. Canarutto, D., Tucci, F., Gattillo, S., Zambelli, M., Calbi, V., Gentner, B., Ferrua, F., Marktel, S., Migliavacca, M., Barzaghi, F., et al. (2021). Peripheral blood stem and progenitor cell collection in pediatric candidates for ex vivo gene therapy: a 10-year series. Mol. Ther. Methods Clin. Dev. *22*, 76–83. https://doi.org/10.1016/J.OMTM.2021.05.013.

72. Biffi, A., Bartolomae, C.C., Cesana, D., Cartier, N., Aubourg, P., Ranzani, M., Cesani, M., Benedicenti, F., Plati, T., Rubagotti, E., et al. (2011). Lentiviral vector common integration sites in preclinical models and a clinical trial reflect a benign integration bias and not oncogenic selection. Blood *117*, 5332–5339. https://doi.org/10.1182/BLOOD-2010-09-306761.

73. Ferrua, F., Cicalese, M.P., Galimberti, S., Giannelli, S., Dionisio, F., Barzaghi, F., Migliavacca, M., Bernardo, M.E., Calbi, V., Assanelli, A.A., et al. (2019). Lentiviral haemopoietic stem/progenitor cell gene therapy for treatment of Wiskott-Aldrich syndrome: interim results of a non-randomised, open-label, phase 1/2 clinical study. Lancet Haematol. *6*, e239–e253. https://doi.org/10.1016/S2352-3026(19)30021-3.

74. Meaker, G.A., and Wilkinson, A.C. (2024). Ex vivo hematopoietic stem cell expansion technologies: recent progress, applications, and open questions. Exp. Hematol. *130*, 104136. https://doi.org/10.1016/J.EXPHEM.2023.12.001.

75. Choi, J.S., and Harley, B.A.C. (2017). Marrow-inspired matrix cues rapidly affect early fate decisions of hematopoietic stem and progenitor cells. Sci. Adv. *3*, e1600455. https://doi.org/10.1126/sciadv.1600455.

76. Kidiyoor, G.R., Li, Q., Bastianello, G., Bruhn, C., Giovannetti, I., Mohamood, A., Beznoussenko, G.V., Mironov, A., Raab, M., Piel, M., et al. (2020). ATR is essential for preservation of cell mechanics and nuclear integrity during interstitial migration. Nat. Commun. *11*, 4828. https://doi.org/10.1038/S41467-020-18580-9.

77. Lamm, N., Read, M.N., Nobis, M., Van Ly, D., Page, S.G., Masamsetti, V.P., Timpson, P., Biro, M., and Cesare, A.J. (2020). Nuclear F-actin counteracts nuclear deformation and promotes fork repair during replication stress. Nat. Cell Biol. *22*, 1460–1470. https://doi.org/10.1038/S41556-020-00605-6.

78. Bastianello, G., Porcella, G., Beznoussenko, G.V., Kidiyoor, G., Ascione, F., Li, Q., Cattaneo, A., Matafora, V., Disanza, A., Quarto, M., et al. (2023). Cell stretching activates an ATM mechano-transduction pathway that remodels cytoskeleton and chromatin. Cell Rep. *42*, 113555. https://doi.org/10.1016/J.CELREP.2023.113555.

79. Lengefeld, J., Cheng, C.W., Maretich, P., Blair, M., Hagen, H., McReynolds, M.R., Sullivan, E., Majors, K., Roberts, C., Kang, J.H., et al. (2021). Cell size is a determinant of stem cell potential during aging. Sci. Adv. *7*, eabk0271. https://doi.org/10.1126/sciadv.abk0271.

80. Florian, M.C., Klose, M., Sacma, M., Jablanovic, J., Knudson, L., Nattamai, K.J., Marka, G., Vollmer, A., Soller, K., Sakk, V., et al. (2018). Aging alters the epigenetic asymmetry of HSC division. PLoS Biol. *16*, e2003389. https://doi.org/10.1371/JOURNAL.PBIO.2003389.

81. Kandi, R., Senger, K., Grigoryan, A., Soller, K., Sakk, V., Schuster, T., Eiwen, K., Menon, M.B., Gaestel, M., Zheng, Y., et al. (2021). Cdc42-Borg4-Septin7 axis regulates HSC polarity and function. EMBO Rep. *22*, e52931. https://doi.org/10.15252/EMBR.202152931.

82. Yang, S., Cai, H., Jin, H., and Tan, W.S. (2008). Hematopoietic reconstitution of CD34+ cells grown in static and stirred culture systems in NOD/SCID mice. Biotechnol. Lett. *30*, 61–65. https://doi.org/10.1007/S10529-007-9517-0.

83. Stephenson, M., and Grayson, W. (2018). Recent advances in bioreactors for cell-based therapies. F1000Res *7*. F1000 Faculty Rev-517. https://doi.org/10.12688/f1000research.12533.1.

84. Bai, T., Li, J., Sinclair, A., Imren, S., Merriam, F., Sun, F., O'Kelly, M.B., Nourigat, C., Jain, P., Delrow, J.J., et al. (2019). Expansion of primitive human hematopoietic stem cells by culture in a zwitterionic hydrogel. Nat. Med. *25*, 1566–1575. https://doi.org/10.1038/s41591-019-0601-5.

85. Marx-Blümel, L., Marx, C., Sonnemann, J., Weise, F., Hampl, J., Frey, J., Rothenburger, L., Cirri, E., Rahnis, N., Koch, P., et al. (2021). Molecular characterization of hematopoietic stem cells after in vitro amplification on biomimetic 3D PDMS cell culture scaffolds. Sci. Rep. *11*, 21163. https://doi.org/10.1038/s41598-021-00619-6.

86. Zhou, D., Chen, L., Ding, J., Zhang, X., Nie, Z., Li, X., Yang, B., and Xu, T. (2020). A 3D engineered scaffold for hematopoietic progenitor/stem cell co-culture in vitro. Sci. Rep. *10*, 11485. https://doi.org/10.1038/s41598-020-68250-5.

87. Li, Y., He, M., Zhang, W., Liu, W., Xu, H., Yang, M., Zhang, H., Liang, H., Li, W., Wu, Z., et al. (2023). Expansion of human megakaryocyte-biased hematopoietic stem cells by biomimetic Microniche. Nat. Commun. *14*, 2207. https://doi.org/10.1038/s41467-023-37954-3.

88. Shah, N.J., Mao, A.S., Shih, T.Y., Kerr, M.D., Sharda, A., Raimondo, T.M., Weaver, J.C., Vrbanac, V.D., Deruaz, M., Tager, A.M., et al. (2019). An injectable bone marrow–like scaffold enhances T cell immunity after hematopoietic stem cell transplantation. Nat. Biotechnol. *37*, 293–302. https://doi.org/10.1038/S41587-019-0017-2.

89. Zandrini, T., Florczak, S., Levato, R., and Ovsianikov, A. (2023). Breaking the resolution limits of 3D bioprinting: future opportunities and present challenges. Trends Biotechnol. *41*, 604–614. https://doi.org/10.1016/j.tibtech.2022.10.009.

90. Jaiswal, S., and Ebert, B.L. (2019). Clonal hematopoiesis in human aging and disease. Science *366*, eaan4673. https://doi.org/10.1126/SCIENCE.AAN4673.

91. Kosicki, M., Tomberg, K., and Bradley, A. (2018). Repair of double-strand breaks induced by CRISPR–Cas9 leads to large deletions and complex rearrangements. Nat. Biotechnol. *36*, 765–771. https://doi.org/10.1038/nbt.4192.

92. Cullot, G., Boutin, J., Toutain, J., Prat, F., Pennamen, P., Rooryck, C., Teichmann, M., Rousseau, E., Lamrissi-Garcia, I., Guyonnet-Duperat, V., et al. (2019). CRISPR-Cas9 genome editing induces megabase-scale chromosomal truncations. Nat. Commun. *10*, 1136. https://doi.org/10.1038/s41467-019-09006-2.

93. Turchiano, G., Andrieux, G., Klermund, J., Blattner, G., Pennucci, V., el Gaz, M., Monaco, G., Poddar, S., Mussolino, C., Cornu, T.I., et al. (2021). Quantitative evaluation of chromosomal rearrangements in gene-edited human stem cells by CAST-Seq. Cell Stem Cell *28*, 1136–1147.e5. https://doi.org/10.1016/j.stem.2021.02.002.

94. Savage, S.A., and Niewisch, M.R. (2023). Dyskeratosis Congenita and Related Telomere Biology Disorders. GeneReviews. https://www.ncbi.nlm.nih.gov/books/NBK22301/.

95. Siegner, S.M., Ugalde, L., Clemens, A., Garcia-Garcia, L., Bueren, J.A., Rio, P., Karasu, M.E., and Corn, J.E. (2022). Adenine base editing efficiently restores the function of Fanconi anemia hematopoietic stem

and progenitor cells. Nat. Commun. *13*, 6900. https://doi.org/10.1038/S41467-022-34479-Z.

96. Schuster, J.A., Stupnikov, M.R., Ma, G., Liao, W., Lai, R., Ma, Y., and Aguila, J.R. (2012). Expansion of hematopoietic stem cells for transplantation: current perspectives. Exp. Hematol. Oncol. *1*, 12. https://doi.org/10.1186/2162-3619-1-12.
97. Shpall, E.J., and Rezvani, K. (2021). Cord blood expansion has arrived. Blood *138*, 1381–1382. https://doi.org/10.1182/BLOOD.2021012725.
98. Milani, M., Fabiano, A., Perez-Rodriguez, M., Hernandez, R.J., Zecchillo, A., Zonari, E., Ottonello, S., Basso-Ricci, L., Canepari, C., Volpin, M., et al. (2025). In vivo haemopoietic stem cell gene therapy enabled by postnatal trafficking. Nature *643*, 1097–1106. https://doi.org/10.1038/s41586-025-09070-3.
99. Ricci, D., Nava, M.M., Zandrini, T., Cerullo, G., Raimondi, M.T., and Osellame, R. (2017). Scaling-Up Techniques for the Nanofabrication of Cell Culture Substrates via Two-Photon Polymerization for Industrial-Scale Expansion of Stem Cells. Materials (Basel) *10*, 66. https://doi.org/10.3390/MA10010066.
100. Zandrini, T., Shan, O., Parodi, V., Cerullo, G., Raimondi, M.T., and Osellame, R. (2019). Multi-foci laser microfabrication of 3D polymeric scaffolds for stem cell expansion in regenerative medicine. Sci. Rep. *9*, 11761. https://doi.org/10.1038/s41598-019-48080-w.
101. Cesana, D., Calabria, A., Rudilosso, L., Gallina, P., Benedicenti, F., Spinozzi, G., Schiroli, G., Magnani, A., Acquati, S., Fumagalli, F., et al. (2021). Retrieval of vector integration sites from cell-free DNA. Nat. Med. *27*, 1458–1470. https://doi.org/10.1038/S41591-021-01389-4.
102. Firouzi, S., López, Y., Suzuki, Y., Nakai, K., Sugano, S., Yamochi, T., and Watanabe, T. (2014). Development and validation of a new high-throughput method to investigate the clonality of HTLV-1-infected cells based on provirus integration sites. Genome Med. *6*, 46. https://doi.org/10.1186/gm568.
103. Spinozzi, G., Calabria, A., Brasca, S., Beretta, S., Merelli, I., Milanesi, L., and Montini, E. (2017). VISPA2: A scalable pipeline for high-throughput identification and annotation of vector integration sites. BMC Bioinform. *18*, 520. https://doi.org/10.1186/s12859-017-1937-9.
104. Berry, C.C., Gillet, N.A., Melamed, A., Gormley, N., Bangham, C.R.M., and Bushman, F.D. (2012). Estimating abundances of retroviral insertion sites from DNA fragment length data. Bioinformatics *28*, 755–762. https://doi.org/10.1093/BIOINFORMATICS/BTS004.
105. Pais, G., Spinozzi, G., Cesana, D., Benedicenti, F., Albertini, A., Bernardo, M.E., Gentner, B., Montini, E., and Calabria, A. (2023). ISAnalytics enables longitudinal and high-throughput clonal tracking studies in hematopoietic stem cell gene therapy applications. Brief. Bioinform. *24*, bbac551. https://doi.org/10.1093/BIB/BBAC551.

STAR★METHODS

KEY RESOURCES TABLE

REAGENT or RESOURCE	SOURCE	IDENTIFIER
Antibodies		
Anti-8-oxo-2'deoxyguanosine	Trevigen	Cat#4354-MC-050; RRID: AB_1857195
Anti-alpha Tubulin antibody – Loading Control	Abcam	Cat#ab4074; RRID: AB_2288001
Anti-human CD11b PE (Clone M1/70)	BioLegend	Cat#101207; RRID: AB_312790
Anti-human CD13 BV421 (Clone WM15)	BD Biosciences	Cat#562596; RRID: AB_2737672
Anti-human CD133/1 PE-Vio 770 (Clone AC133)	Miltenyi Biotec	Cat#130-113-110; RRID: AB_2725939
Anti-human CD14 APC-Cy7 (Clone M5E2)	BioLegend	Cat#301820; RRID: AB_493695
Anti-human CD15 BV510 (Clone W6D3)	BioLegend	Cat#323028; RRID: AB_2563400
Anti-human CD19 BV510 (Clone HIB19)	BioLegend	Cat#302242; RRID: AB_2561668
Anti-human CD235a (GlyA) APC (Clone GA-R2 (HIR2))	BD Biosciences	Cat#551336; RRID: AB_398499
Anti-human CD3 PE (Clone OKT3)	BioLegend	Cat#317308; RRID: AB_571913
Anti-human CD33 BV421 (Clone WM53)	BD Biosciences	Cat#562854; RRID: AB_2737405
Anti-human CD33 PE-Cy7 (Clone P67.6)	BD Biosciences	Cat#333952; RRID: AB_2713932
Anti-human CD34 PE (Clone AC136)	Miltenyi Biotec	Cat#130-113-179; RRID: AB_2726006
Anti-human CD34 PE-Cy7 (Clone 8G12)	BD Biosciences	Cat#348811; RRID: AB_2868855
Anti-human CD38 PerCP-Cy5.5 (Clone HB-7)	BioLegend	Cat#356614; RRID: AB_2562183
Anti-human CD41 PE-Cy5 (Clone HIP8)	BioLegend	Cat#303708; RRID: AB_314378
Anti-human CD45 APC-eFluor 780 (Clone HI30)	Invitrogen	Cat#47-0459-42; RRID: AB_1944368
Anti-human CD45 PE-Cy7 (Clone HI30)	BioLegend	Cat#304016; RRID: AB_314404
Anti-human CD45Ra Alexa Fluor 700 (Clone HI100)	BioLegend	Cat#304120; RRID: AB_493763
Anti-human CD56 Pacific Blue (Clone MEM-188)	BioLegend	Cat#304629; RRID: AB_2282499
Anti-human CD8 PE-Cy7 (Clone RPA-T8)	BD Biosciences	Cat#557746; RRID: AB_396852
Anti-human CD90 APC (Clone 5E10)	BD Biosciences	Cat#559869; RRID: AB_398677
Anti-human FCR Blocking	Miltenyi Biotec	Cat#130059901; RRID: AB_2892112
Anti-human p38-MAPK pThr180/pTyr182	Cell Signalling	Cat#9211; RRID: AB_331641
Donkey anti-mouse IgG (H+L) Secondary Antibody, Alexa Fluor 488	Thermo Fisher Scientific	Cat#A-21202; RRID: AB_141607
Donkey anti-mouse IgG (H+L) Secondary Antibody, Alexa Fluor 647	Thermo Fisher Scientific	Cat#A-31571; RRID: AB_162542
Donkey anti-rabbit IgG (H+L) Secondary Antibody, Alexa Fluor 568	Thermo Fisher Scientific	Cat#A-10042; RRID: AB_2534017
Mouse anti-human Phospho-Histone H2A.X (Ser139) (Clone JBW301)	Merck Millipore	Cat#05-636; RRID: AB_309864
Purified Rat anti-mouse CD16/CD32 (Clone 2.4G2)	BD Biosciences	Cat#553141; RRID: AB_394656
Rabbit anti-human phospho-RPA32 (S33)	Bethyl Laboratories	Cat#A300-246A; RRID: AB_2180847
Biological samples		
Umbilical cord blood	San Raffaele Hospital	N/A
Leukapheresis from WAS patients	San Raffaele Hospital	N/A
Mobilized peripheral blood	Mobilized Leukopak (AllCells)	N/A

(*Continued on next page*)

Continued

REAGENT or RESOURCE	SOURCE	IDENTIFIER
Chemicals, peptides, and recombinant proteins		
16,16-Dimethyl Prostaglandin E2	Cayman Chemical	Cat#14750
7-AAD Viability Staining solution	Biolegend	Cat#420403
ABE8.20-m	Fiumara et al.	N/A
Alt-R CRISPR-Cas9 Negative Control crRNA #1	Integrated DNA Technologies	Cat#1072544
Cas9 enhancing	Integrated DNA Technologies	Cat#1075916
CellROX™ Deep Red Reagent	Thermo Fisher	Cat#C10422
CometAssay LMAgarose	R&D Systems	Cat#4250-050-02
Corning® Collagen I	Sigma-Aldrich	Cat#CLS354236-1EA
CometAssay Lysis Solution	R&D Systems	Cat#4250-050-01
DAPI	Sigma-Aldrich	Cat#D9542
Erythropoietin (EPO, Eprex)	Janssen-Cilag	N/A
gRNA *AAVS1*	Schiroli et al.	N/A
gRNA *B2M* exon 1	Fiumara et al.	N/A
GSE56 and Ad5-E4orf6/7	Ferrari et al.	N/A
Hoechst 3342 Fluorescent Stain	Thermo Fisher	Cat#62249
Human GM-CSF	Miltenyi Biotec	Cat#130-093-862
Human IL-11	Miltenyi Biotec	Cat#130-103-439
Human IL-2	Miltenyi Biotec	Cat#130097743
Human IL-3 recombinant protein	Peprotech	Cat#200-03
Human IL-7	Miltenyi Biotec	Cat#130-095-363
Human Low-Density Lipoproteins (LDL)	Stem Cell Technologies	Cat#02698
Intracellular Staining Permeabilization Wash Buffer	Biolegend	Cat#421002
Liberase™	Sigma-Aldrich	Cat#5401119001
nicking gRNA 5 *B2M* exon 1	Fiumara et al.	N/A
Pacific Blue Annexin V	Biolegend	Cat#640918
Paraformaldehyde solution 4% in PBS	Santa Cruz Biotechnology	Cat#SC-281692
PE3max	Fiumara et al.	N/A
pegRNA 5 *B2M* exon 1	Fiumara et al.	N/A
Poly-L-lysine solution	Sigma-Aldrich	Cat#P8920
Recombinant human Flt3-Ligand	Peprotech	Cat#300-19
Recombinant human IL6	Peprotech	Cat#200-06
Recombinant human stem cell factor (SCF)	Peprotech	Cat#300-07
Recombinant human thrombopoietin (TPO)	Peprotech	Cat#300-18
SpCas9 Nuclease	Aldevron	Cat#9212
StemRegenin 1 (SR1)	Biovision	Cat#1967
UM171	STEMCell Technologies	Cat#72914
Critical commercial assays		
CellTrace™ Violet Cell Proliferation Kit	Thermo Scientific	Cat# C34557
Click-iT EdU Pacific Blue Flow cyometry assay kit	Thermo Fisher	Cat#C10418
ddPCR Supermix for Probes (No dUTP)	BioRad	Cat #1863024
ddPCR™ Copy Number Assay: TTC5, Human, Homo sapiens	BioRad	Cat# 12017424
GoTaq Flexi DNA Polymerase	Promega Corporation	Cat#M8295
P3 Primary Cell 4D-Nucleofector X Kit S	Lonza	Cat#V4XP-3032
QIAamp DNA Micro Kit	QIAGEN	Cat#56304

(*Continued on next page*)

Continued		
REAGENT or RESOURCE	SOURCE	IDENTIFIER
QIAamp DNA Mini Kit	QIAGEN	Cat#51304
QX200™ ddPCR™ EvaGreen Supermix	BioRad	Cat#1864034
RNase-free DNase Set	QIAGEN	Cat#79254
RNeasy Plus Micro Kit	QIAGEN	Cat#74034
T7 endonuclease 1	New England Biolabs	Cat#M0302L
Deposited data		
Integration site analysis	This paper	https://github.com/calabrialab/Code_3D_Scaffold
RNA sequencing	This paper	https://www.ncbi.nlm.nih.gov/geo/query/acc.cgi?acc=GSE280536
Experimental models: Cell lines		
Human cord blood CD34+ Stem/Progenitor cells	Lonza	Cat#2C-101
Experimental models: Organisms/strains		
NOD.CG- Prkdc^{scid}Il2rg^{tm1Wjl}/SzJ (NSG) *Mus Musculus*	Charles River Laboratories (IACUC: #1385)	RRID: IMSR_JAX:005557
Oligonucleotides		
See METHOD DETAIL	This paper	N/A
Recombinant DNA		
AAV6.GFP	Schiroli et al.	N/A
LV.GFP	Zonari et al.	N/A
LV.WAS	Ferrua et al.	N/A
Software and algorithms		
BD FACSDiva software	BD Biosciences	https://www.bdbiosciences.com/en-us/products/software/instrument-software/bd-facsdiva-software
CaspLab	CaspLab	https://sourceforge.net/projects/casp/
FlowJo	FlowJo	https://www.flowjo.com/
ImageJ (v2.9)	NIH	https://imagej.nih.gov/ij/
LAS X Leica Software	Leica Mycrosystems	https://www.leica-microsystems.com/it/prodotti/software-per-microscopi/p/leica-las-x-ls/
Prism software (v10)	GraphPad Prism	https://www.graphpad.com/
QuantaSoft (v1.7)	Biorad	https://www.bio-rad.com/
R statistical software	R Project	https://www.r-project.org/
Vision 4D arivis pro	ZEISS	https://kb.arivis.com/vision4d-arivis-pro
Other		
Nichoids	Politecnico di Milano	N/A
Spongostan	Ferrosan Medical Devices	CAT# MS0005

EXPERIMENTAL MODEL AND STUDY PARTICIPANTS DETAILS

Mice

NOD-SCID-IL2rg$^{-/-}$ (NSG) female mice were purchased from Charles River Laboratories and maintained in specific pathogen-free conditions. The procedures involving animals were designed and performed with the approval of the Animal Care and Use Committee of the San Raffaele Hospital and communicated to the Ministry of Health and local authorities according to Italian law (IACUC #1385). Mice sample size was determined in accordance with ethical regulations and the 3Rs principles. Mice were randomly assigned to each experimental group.

Primary stem cell cultures

Cord blood-derived CD34+ HSPCs: Cells were either freshly purified from human CB after obtaining informed consent and upon approval by the San Raffaele Hospital ethical committee or purchased frozen from Lonza or StemExpress. HSPCs were cultured in serum-free StemSpan SFEM medium (StemCell Technologies) supplemented with 2mM L-glutamine and Penicillin-Streptomycin (100IU/ml penicillin, 100mg/ml streptomycin), 1μM SR-1 (Biovision), 50nM UM171 (STEMCell Technologies), and recombinant human cytokines (100ng/ml SCF, 100ng/ml FLT3-L, 20ng/ml TPO, and 20ng/ml IL-6; Peprotech). 10μM 16,16-Dimethyl Prostaglandin E2 (Cayman) was added only at thawing.

Mobilized peripheral blood-derived CD34+ HSPCs: Cells were purified in-house with the CliniMACS CD34 Reagent System (Miltenyi Biotec) from Mobilized Leukopak (AllCells, mobilized with G-CSF or G-CSF+Plerixafor) according to the TIGET-HPCT protocol approved by OSR Ethical Committee and following the manufacturer's instructions. HSPCs were cultured in serum-free StemSpan SFEM medium (StemCell Technologies) supplemented with 2mM L-glutamine and Penicillin-Streptomycin (100IU/ml penicillin, 100mg/ml streptomycin), 1μM SR-1(Biovision), 35nM UM17 (STEMCell Technologies), and recombinant human cytokines (300ng/ml SCF, 300ng/ml FLT3-L, and 100ng/ml TPO; Peprotech). 10μM 16,16-Dimethyl Prostaglandin E2 (Cayman) was added only at thawing, only for GE strategies.

Wiskott-Aldrich Syndrome-derived CD34+ HSPCs: Cells were purified with human CD34 MicroBead Kit (Miltenyi Biotec) from excess material obtained from G-CSF+Plerixafor leukapheresis from patients undergoing gene therapy in the Pediatric immunohematology unit in the San Raffaele Hospital after obtaining informed consent and upon approval by the San Raffaele Hospital ethical committee (protocol TIGET-09). HSPCs were cultured in SCGM medium (CellGenix/Sartorius) supplemented with Penicillin-Streptomycin (100IU/ml penicillin, 100mg/ml streptomycin) and recombinant human cytokines (100ng/ml TPO, 60ng/ml IL3, 300ng/ml SCF, and 300ng/ml FLT3-L; CellGenix/Sartorius). Only for the 2D condition, coating with retronectin (Takara) was performed according to the manufacturer's instructions. GMP-grade reagents were provided by Marina Radrizzani's group.

Cell seeding on nichoids: In this study, 1-5$\times10^5$ cells were seeded in a single nichoid in the current configuration fabricated on a 12 mm slide. To avoid over-confluency, multiple nichoids per donor were used when requiring a larger number of cells. Specifically, 1-5$\times10^5$ cells were resuspended in 100μl of fresh media upon thawing and placed directly on top of the nichoid without directly touching the scaffold. Cells were left seeding for 30-45 min and then topped up with 400μl of culture media.

Cell seeding on spongostan scaffolds: spongostan (Ferrosan Medical Devices) was obtained in sterile single cubes of 1$\times$1$\times$1cm and then cut into cylinders of 3.5mm in height and 4mm in diameter, as previously described[70]. Specifically, 2$\times10^5$ cells were resuspended in 20μl of fresh media upon thawing and placed directly on top of the scaffold positioned in the bottom of a 1.5ml tube. Cells were left seeding for 2h to allow complete absorption of the medium and cell infiltration, and then topped up with 500μl of culture media. The tube containing the scaffold was subsequently placed in the incubator with the cap left open to allow adequate gas exchange, while sterility was maintained by covering the opening with a sterile 0.45μm filter.

Cell seeding on spheroids: 300μl of collagen solution was prepared on ice with 205μl of culture media, 9μl of 10X PBS, 2μl of 1M NaOH, and 84μl of rat tail collagen I (Corning) and used immediately after preparation, as previously described[69] Specifically, 3$\times10^5$ cells were resuspended in 30μl of collagen solution, and 5μl of cell suspension were spotted as hanging drops (6 per donor) on the lid of a Petri dish. After 30 min of incubation to promote collagen polymerization, spheroids were transferred to a cell culture plate with 2ml of culture media.

Cell recovery from nichoids and spongostan scaffolds: Briefly, culture medium was gently removed, and scaffolds were covered with 500μl citrate solution (0.015M sodium citrate, 0.135M KCl in sterile H2O). Cells were incubated for 15 min in the incubator and then recovered by gently pipetting close to the scaffold. After a second quick wash with citrate solution, the cellular suspension was diluted in DPBS, pelleted, and resuspended in the appropriate volume of culture medium.

Cell recovery from spheroids: Spheroids were collected and digested in 90μl of Liberase solution (0.3mg/mL in FBS, Sigma-Aldrich) in a thermomixer at 37°C for 10 min at 900rpm. The cellular suspension was diluted in DPBS, pelleted, and resuspended in the appropriate volume of culture medium.

All cells were cultured in a 5% CO_2 humidified atmosphere at 37°C. Equal numbers of cells were used to perform head-to-head comparisons between 2D- and 3D-cultured HSPCs, counted by Trypan Blue exclusion. Detailed cell numbers and cell viability across donors and experiments are reported in Table S1.

METHOD DETAILS

Nichoids fabrication

Nichoids were provided by Manuela Teresa Raimondi's group (Politecnico di Milano) and fabricated as described in previous works[99] using two-photon polymerization of the SZ2080 biocompatible resin on a circular borosilicate glass coverslip (170μm in thickness and 12mm in diameter, Bio Optica). The resin's two-photon absorption cross-section was enhanced by adding the commercial photoinitiator, Irgacure-369. SZ2080 was chosen for its mechanical properties, low cytotoxicity, and low autofluorescence.[100] A cavity-dumped femtosecond laser with a 1030nm wavelength, pulse duration under 400fs, and 1MHz repetition rate was focused into the photosensitive material through a high-magnification oil-immersion microscope objective (100X, 1.4 numerical aperture, Plan-Apochromat, Carl Zeiss). Three fast linear stages (two horizontal and one vertical, ANT130, Aerotech) were used to move the sample across the laser beam, enabling continuous polymerization over the entire substrate. A translation velocity of 3mm/s was set.

The nichoid structure comprised two perpendicular sets of six parallel lines, 90×90μm in transverse dimensions, and consisted of a lattice of interconnected lines, with a graded spacing between 10 and 30μm transversely and a uniform spacing of 15μm vertically. 30μm tall columns were placed at each line crossing to provide structural support. Nichoids were arranged in 5x5-unit blocks, sharing side walls, and the entire glass substrate was covered by these blocks, separated by 30μm corridors. Following the fabrication process, samples underwent development in a 50% (v/v) 2-pentanone and 50% (v/v) isopropyl alcohol solution to eliminate unirradiated photoresist, washed with clean isopropyl alcohol, and dried with nitrogen.

To ensure sterility before cell culture, nichoids were covered with 70% EtOH solution for at least 3h, washed three times with ddH2O, and exposed to UV-C irradiation for at least 30 min.

Images of the nichoid culture substrate by scanning electron microscopy (SEM, Phenom Pro, Phenom-World) were provided by Politecnico di Milano.

Genetic engineering

The initial number of cells subject to genetic engineering was equal for the 2D and 3D conditions but variable between experiments, depending on the number of cells required for downstream analyses (Table S1). For genome editing, 1–7.5×10^5 cells were generally electroporated in a single 16-well nucleocuvette strip (larger numbers of cells were divided in multiple nucleocuvette wells).

Cas9/AAV6

After three days of *ex vivo* culture, cells were nucleofected with 2.5–1.25μM of ribonucleoproteins (RNPs) and electroporation enhancer (Integrated DNA Technologies) according to the manufacturer's instructions using P3 Primary Cell 4D-Nucleofector X Kit and program EO-100 (Lonza). RNPs were assembled by incubating for 10 min at room temperature at 1:1.5 molar ratio S.p. Cas9 protein (Aldevron) with synthetic gRNAs (Integrated DNA Technologies) targeting the *AAVS1* locus[24] (sequence: GTCACCAATCCTGTCCCTAG). Transduction with AAV6 (purchased from AAV vector core, TIGEM) was performed at a dose of 1×10^4 vg/cell after electroporation. The design of AAV6 donor templates encoding for a PGK.GFP reporter cassette with homologies for the *AAVS1* locus was previously reported.[24] GSE56-Ad5-E4orf6/7 mRNA was provided by Luigi Naldini's group.[34] Editing efficiency was assessed by FACS analyses, digital droplet PCR (ddPCR), and T7 endonuclease 1 assay.

Base-editing

After three days of *ex vivo* culture, cells were nucleofected with 75pmol of synthetic gRNA (Synthego) targeting the exon 1 of *B2M* (sequence: GAGTAGCGCGAGCACAGCTA) and 3.5μg of ABE8.20-m optimized RNA (provided by Luigi Naldini's group)[25] according to the manufacturer's instructions using P3 Primary Cell 4D-Nucleofector X Kit and program EO-100 (Lonza). Editing efficiency was assessed by FACS analyses using anti-human B2M FITC (BioLegend) and Sanger Sequencing.

Prime-editing

After three days of *ex vivo* culture, cells were nucleofected with 186 pmol of *B2M* pegRNA (Integrated DNA Technologies, sequence: mG*mA*mG*UAGCGCGAGCACAGCUAGUUUUAGAGCUAGAAAUAGCAAGUUAAAAUAAGGCUAGUCCGUUAUCAACUUGAAAAAGUGGCACCGAGUCGGUGCUCCGUGGCCUGAGCUGUGCUCGCGCUmU*mU*mU), 75pmol of synthetic gRNA (Synthego) targeting the exon 1 of *B2M* (sequence: AGTGGAGGCGTCGCGCTGGC), and 7.5μg of PEmax optimized mRNA (provided by Luigi Naldini's group)[25] according to the manufacturer's instructions using P3 Primary Cell 4D-Nucleofector X Kit and program EO-100 (Lonza). Editing efficiency was assessed by FACS analyses using anti-human B2M FITC (BioLegend) and Sanger Sequencing.

Lentiviral gene addition

According to the experimental design described in the main text, cells were transduced for 14h with third-generation self-inactivating lentiviruses encoding for a PGK.GFP reporter cassette[37] or WASP under the control of a 1.6 kb reconstituted WAS promoter (two rounds of transduction; GMP-grade vector, provided by Marina Radrizzani's group).[73] 10μM 16,16-Dimethyl Prostaglandin E2 (Cayman) was added 2h prior to transduction. 8μM Cyclosporine H (Sigma-Aldrich) was added together with 16,16-Dimethyl Prostaglandin E2 (Cayman). Gene transfer efficiency was assessed by FACS analyses and ddPCR.

Functional assays

Colony-forming unit cell assay

CFU-C assay was performed by plating 800 or 5000 cells (from *ex vivo* culture or upon isolation from the bone marrow of transplanted mice, respectively) in methylcellulose-based medium (MethoCult H4434, StemCell Technologies) supplemented with Penicillin-Streptomycin (100IU/ml penicillin, 100mg/ml streptomycin). Three technical replicates were performed for each sample, and the mean value was plotted and used for statistical analysis. Two weeks after plating, colonies were counted in a blinded fashion. Erythroid, myeloid, and mixed colonies were identified according to morphological criteria. Representative pictures were acquired with the STEMvision Instrument.

Myeloid-Erythroid-Megakaryocyte (MEM) single-cell differentiation assay

CD34+CD133+CD45RA−CD90+ population (negative to ZombieAqua viable dye) was sorted as single cells (1 cell/well) and seeded in U-bottom 96-well filled with 100 μl/well MEM cytokine medium[52]: StemPro medium with nutrients supplement (Life Technologies) supplemented with 2mM L-glutamine and Penicillin-Streptomycin (100IU/ml penicillin, 100mg/ml streptomycin), recombinant human cytokines (100ng/ml SCF, 20ng/ml Flt3-L, 100ng/ml TPO, 50ng/ml IL-6, 10ng/ml IL-3, 50ng/ml IL-11, 20ng/ml GM-CSF, 10ng/ml IL-2, 20ng/ml IL-7; Miltenyi Biotec), 3UI/ml erythropoietin (Eprex, Janssen-Cilag), and 50ng/ml h-LDL (Stem Cell Technologies). Cell sorting was performed with BD FACSAria Fusion (BD Biosciences); cells were sorted with a 100μm nozzle.

Xenotransplantation studies

Xenotransplantation studies were performed on 6/10-weeks-old NSG female mice by intravenous injection after sub-lethal irradiation (150–180 cGy). Up to six different HSPC donors were pooled at thawing, and the resulting pool of cells was split between the 2D and 3D conditions for transplantation, except in the WAS-related experiment, for which the two patients were kept separated. Pooling was performed to reach sufficient numbers of cells for transplantation and to generate a more uniform input population while still preserving a degree of donor-derived diversity, offering a more representative model than single-donor samples. Different pools of donors were used to perform each transplantation experiment presented in the manuscript.

The number of cells transplanted into each mouse is reported as follows: 1×10^5 CB-derived CD34+ cells for non-genetically manipulated HSPCs, 5×10^5 CB-derived CD34+ cells for Cas9/AAV6 + GSE56 and Ad5-E4orf6/7 edited HSPCs, 4×10^5 mPB-derived CD34+ cells for LV-transduced HSPCs, and 4-5×10^5 cells (depending on the donor) for WAS patient-derived HSPCs.

For secondary transplantation of Cas9/AAV6 + GSE56 and Ad5-E4orf6/7 edited HSPCs, CD34+ cells purified from the BM of primary recipients were pooled according to the experimental group, and 1×10^6 cells were then injected intravenously into each mouse.

Human engraftment and the presence of engineered cells were monitored through FACS analyses by serial collection of blood from the mouse tail, and bone marrow and spleen (at endpoint).

Molecular analyses

Digital droplet PCR

Genomic DNA was isolated with QIAamp DNA Mini or Micro Kit (QIAGEN), and ddPCR was performed using the QX200 Droplet Digital PCR System (Biorad) according to the manufacturer's instructions.

For HDR-editing with Cas9/AAV6, 10ng of genomic DNA was analyzed with ddPCR Supermix for Probes (BioRad). Primers and probes were designed between the HDR donor template sequence and the 3' integration junction on the target AAVS1 locus (FW: GATTGGGAAGACAATAGCAG; REV: TCTTGGGAAGTGTAAGGAAG; probe: CCAGATAAGGAATCTGCCTA). The TTC5 gene was used as the control sequence, and the respective primers and probes were purchased in the PrimePCR ddPCR Copy Number Assay: TTC5, Human (BioRad). The different probes were conjugated with FAM (target) and HEX (TTC5 reference) fluorophores. Thermal conditions for annealing and extension were adjusted as follows: 95°C x 10 min; 94°C x 30 sec, 55°C x 1 min, 72°C x 2 min (40 cycles); 98°C x 10 min.

For VCN analyses, 10ng of genomic DNA was analyzed with EvaGreen Supermix (BioRad). Primers were designed to amplify only integrated LV (FW: TCACTCCCAACGAAGACAAGATC; REV: GAGTCCTGCGTCGAGAGAG), normalized using the *TERT* (FW: GGCACACGTGGCTTTTCG; REV: GGTGAACCTCGTAAGTTTATGCAA) gene as a control sequence, as previously reported.[35] Thermal conditions for annealing and extension were adjusted as follows: 95°C x 5 min; 95°C x 30 sec, 63°C x 1 min (40 cycles); 4°C x 5 min; 90°C x 5 min.

T7 endonuclease 1 assay

Genomic DNA from Cas9/AAV6-edited cells purified for ddPCR analysis was used to measure non-homologous end joining (NHEJ) efficiency through the mismatch-sensitive T7 endonuclease 1 (New England Biolabs) assay by PCR-based amplification of the targeted locus, followed by digestion, as previously reported[24] and according to the manufacturer's instructions. PCR amplification was performed with GoTaq Flexi DNA Polymerase (Promega Corporation) using primers specific for *AAVS1* (FW: CTTCAGGACAGCATGTTTGC, REV: ACAGGAGGTGGGGGTTAGAC) with thermal conditions for annealing and extension adjusted as follows: 95°C x 10 min; 95°C x 30 sec, 61°C x 30 sec, 72°C x 90 sec (40 cycles); 72°C x 10 min; 90°C x 5 min. PCR product was then denatured and annealed as follows: 95°C x 10 min; 95°C to 85°C x -2°C/sec; 85°C to 25°C x -0.1°C/sec. Samples were then digested according to the manufacturer's instructions. Digested DNA fragments were resolved and quantified by capillary electrophoresis on a 4200 TapeStation System according to the manufacturer's instructions.

Sanger Sequencing

Genomic DNA was isolated with QIAamp DNA Mini or Micro Kit (QIAGEN). 50-100ng of DNA was amplified by PCR using primers for the *B2M* exon 1, as previously reported[25] (FW: CGCGTTTAATATAAGTGGAGGC; REV: GGAGAACTTGGAGAAGGGAAGT). Thermal conditions for annealing and extension were adjusted as follows: 95°C x 10 min; 95°C x 30 sec, 59°C x 30 sec, 72°C x 30 sec (40 cycles); 72°C x 10 min. Afterward, PCR amplicons were purified using AMPure XP Beads (Beckman Coulter) according to the manufacturer's instructions. 10ng of purified PCR products were sequenced using the REV primer. Sequencing data were analyzed with the online tool EditR.

Flow cytometry

Immunophenotypic and apoptosis analysis

For immunophenotypic analyses of *ex vivo* cultured HSPCs, 3–10×10^4 cells were washed with 2% FBS in DPBS and stained with the following fluorescent-labeled antibodies (1:100 dilution, each) for 15 min at 4°C: anti-human CD34 PE (Miltenyi Biotec), anti-human CD133 PE-Vio 770 (Miltenyi Biotec), and anti-human CD90 APC (BD Biosciences). Cells were washed in 2% FBS in DPBS. Where indicated, immunophenotypic staining was combined with Annexin V (BioLegend) and 7-amino-actinomycin D (7-AAD) (BioLegend) viability staining according to the manufacturer's instructions (3 and 1μl *per* sample, respectively).

For immunophenotypic analyses of cells retrieved from *in vivo* organs, blood samples and purified cells were washed with 2% FBS in DPS and incubated with anti-human and anti-mouse FcR Blocking (1:100 and 1:200 dilution, respectively; Miltenyi Biotec) for 10 min at room temperature. Then, cells were stained with combinations of the following fluorescent-labeled antibodies (1:100

dilution, each) for 15 min at 4°C: anti-human CD45 APC-eFluor 780 (Invitrogen), anti-human CD19 BV510 (BD Biosciences), anti-human CD13 BV421 (BD Biosciences), anti-human CD33 PE-Cy7 (BD Biosciences), anti-human CD3 PE (BioLegend), anti-human CD8 APC (BioLegend), and anti-human CD34 PE-Cy7 (BD Biosciences). Cells were washed in 2% FBS in DPBS. 7-AAD was employed as a viability stain.

Sample acquisition was performed with FACSCanto II (BD Biosciences). Single-stained and Fluorescence Minus One (FMO) stained cells were used as controls, and SPHERO™ Rainbow Calibration Particles (Spherotech) were used to perform instrument calibration. Data were analyzed using the FlowJo software.

MEM single-cell differentiation assay analysis

All single-cell-derived colonies were stained directly into 96 U-bottom plates. Cells were washed with 100 μl/well 2% FBS in DPBS and then stained with 50 μl/well of the following antibody mix: anti-human CD45-PECy7 (1:300; BioLegend), anti-human CD11b-PE (1:500; BioLegend), anti-human CD41-PECy5 (1:200; BioLegend), anti-human GlyA-APC (1:1000; BD Biosciences), anti-human CD14-APCCy7 (1:500; BioLegend), anti-human CD56-BV421 (1:200; BioLegend), and anti-human CD15-BV510 (1:1000; BioLegend) for 20 min at room temperature and then washed with 100 μl/well 2% FBS in DPBS + 2% FBS. Samples acquisition was performed by high-throughput flow cytometry with FACSCanto II (BD Biosciences). Colonies were considered only if composed of $\geq$ 30 cells.

Proliferation analysis with CellTrace Violet

Immediately after thawing, HSPCs were stained with Cell Trace Violet (Thermo Fisher Scientific) following the manufacturer's instructions. Cells were resuspended in DPBS at a concentration of $1x10^6$/ml, and 1μl of Cell Trace solution was added to each ml of cell suspension for a final concentration of 5μM. Cells were incubated for 20 min in the incubator at 37°C and then for 5 min with five times the original staining volume of 2% FBS in DPBS. After centrifugation, cells were resuspended in the appropriate culture medium volume. After at least 30 min, samples were acquired with FACSCanto II (BD Biosciences) to check the effectiveness of the staining. Proliferation analyses were subsequently performed on day 7. Data were analyzed using the FlowJo software.

CellROX staining

CellRox (Thermo Fisher Scientific) was pre-diluted in DMSO according to the manufacturer's instructions. 1μM CellROX was directly added to the cell culture ($3\text{-}10\times10^4$ cells). Cells were incubated for 40 min in the incubator at 37°C. After washing in 2% FBS in DPBS, samples were immediately acquired with FACSCanto II (BD Biosciences). Data were analyzed using the FlowJo software.

8-oxo-2'-deoxyguanosine staining

$3\text{-}10x10^4$ cells were washed with 2% FBS in DPBS and fixed with 4% paraformaldehyde (Santa Cruz Biotechnology) at room temperature for 15 min. Cells were washed again and denatured with 100 μl of HCl (2N) for 20 min at room temperature. After washing with 2% FBS in DPBS, cells were permeabilized with 800μl of 1X Intracellular Staining Permeabilization Wash Buffer (BioLegend) for 20 min at room temperature. Then, cells were washed with 2% FBS in DPBS and stained with 8-oxo-2'-deoxyguanosine Antibody (1:250 dilution) (Bio-Techne) at 4°C overnight. After washing with 2% FBS in DPBS, samples were stained with anti-mouse secondary antibody Alexa Fluor 488 (1:1000 dilution) (Thermo Fisher Scientific) for 45 min at room temperature. Cells were washed with 2% FBS in DPBS, and sample acquisition was performed with FACSCanto II (BD Biosciences). Data were analyzed using the FlowJo software.

Phospho-p38 staining

$3\text{-}10x10^4$ cells were washed with 2% FBS in DPBS, eventually stained with surface markers, and fixed with 4% paraformaldehyde (Santa Cruz Biotechnology) at room temperature for 15 min. Cells were washed again with 2% FBS in DPBS and permeabilized with 100μl of 1X Click-iT saponin-based permeabilization at room temperature for 15 min. Then, cells were stained with phospho-p38 MAPK antibody (1:100 dilution) (pThr180/pTyr182; Cell Signalling) at 4°C overnight. After washing with 2% FBS in DPBS, samples were stained with anti-rabbit secondary antibodies (1:1000 dilution) (Alexa Fluor 488 or Alexa Fluor 647; Thermo Fisher Scientific) for 45 min at room temperature. After washing with 2% FBS in DPBS, sample acquisition was performed with FACSCanto II (BD Biosciences), and the collected data were analyzed using the FlowJo software.

Cell cycle analysis

Cell cycle analyses were performed by Click-iT EdU Alexa Fluor PacificBlue Imaging Kit (Thermo Fisher Scientific) and Hoechst (Thermo Fisher Scientific) staining. $3\text{-}10x10^4$ cells were treated with 2μM 5-ethynyl-2′-deoxyuridine (EdU) for 4 hours in culture. Then, cells were washed with 2% FBS in DPBS and fixed with 100μl of Click-iT fixative for 15 min at room temperature. Cells were washed again and permeabilized with 100μl of 1X Click-iT saponin-based permeabilization for 15 min at room temperature. EdU was marked by incubating cells with 500μl of Click-iT Plus reaction cocktail for 30 min at room temperature. Finally, cells were washed and stained with 2μM Hoechst overnight at 4°C. After the incubation, sample acquisition was performed with FACSymphony A5 SORP (BD Biosciences). Data were analyzed using the FlowJo software.

Immunofluorescence analysis

For the analyses of γH2AX and pRPA DDR sensors: multitest slides (MP Biomedicals) were treated with poly-L-lysine solution (Sigma-Aldrich) at 1mg/ml concentration for 20 min at room temperature. After two washes with DPBS solution, approximately $3\text{–}10x10^4$ cells were seeded on covers for 20 min and fixed with 4% paraformaldehyde (Santa Cruz Biotechnology) for another 20 min. After washing, cells were then permeabilized with 0.3% Triton X-100 for 15 min at room temperature. After blocking with 0.5% BSA and 0.2% fish gelatin in DPBS for 30 min, cells were probed with anti-phospho Histone H2A.X (1:200 dilution; Ser139, clone JBW301; Merk) and phospho-RPA32 (1:200 dilution; S33; Bethyl Laboratories) for 1h at room temperature. After primary antibodies incubation, cells were washed three times with blocking solution and incubated with Alexa 488-, 568- and/or 647-labeled

secondary antibodies (1:1000 dilution) for 45 min at room temperature (Thermo Fisher Scientific). Nuclear DNA was stained with 0.2mg/ml DAPI (Sigma-Aldrich), and covers were mounted with Aqua-Poly/Mount solution (Polysciences Inc.) on glass slides (Bio-Optica). Fluorescent images were acquired using a Leica SP5 Confocal microscope. Foci quantification was performed with the ImageJ software. For the analysis of HSPC morphology and tubulin distribution, cells were fixed directly on nichoids, spongostan-made scaffolds, spheroids, or coverglasses (Bio Optica) on day 7 of *ex vivo* culture with 4% paraformaldehyde (Santa Cruz Biotechnology) for 20 min at room temperature. To remove PAF residues and to diminish cell autofluorescence, samples were incubated for 5 min with 0.1M glycine solubilized in PBS. Cells were permeabilized with 0.25% Triton-X-100 in PBS solution for 10 min at room temperature. After blocking with 2% BSA in 0.1%Tween20 solution for a few hours (up to 4), cells were incubated overnight and at 4°C, with anti-alpha tubulin primary antibody (1:200 dilution; Abcam) diluted in a 0.1%Tween20 solution. Samples were washed three times in PBS and then incubated with Alexa 488-labeled secondary antibodies (1:1000 dilution, Abcam) for 45 min at room temperature. Cell nuclei were labelled with 1 mg/ml Hoechst 33342 (Thermo Fisher Scientific) for 15 min at room temperature. Finally, after washing twice in PBS and once in ddH2O, samples were mounted in Mowiol (Sigma-Aldrich). Samples were acquired using a Nikon AR1+ confocal microscope (60X oil immersion objective, 1.4NA 0.13WD, pinhole set to 0.9 Airy Units) or an Olympus fluoVIEW FV3000RS Confocal microscope (60X oil immersion objective, pinhole set to 1 Airy Units). 1024X1024 pixel images were acquired as z-stack images, with a 0.3mm step. Fluorescent images were analyzed with ImageJ and Arivis Vision4D.

Comet assay

HSPCs were suspended at 1 x 10^5 cells/ml in ice-cold DPBS and mixed with molten Comet LMAgarose (Trevigen, MD) at a ratio of 1:10 (v/v) and immediately pipetted onto CometSlides (Trevigen, MD) and placed for 30 min at 4°C. Once solidified, slides were immersed in pre-chilled Lysis Solution (Trevigen, MD) for 1 hour at 4°C. Following lysis, slides were immersed in freshly prepared alkaline unwinding solution pH > 13 (300 mM NaOH, 1mM EDTA) for 1 hour at 4°C and then electrophoresed in alkaline electrophoresis solution pH > 13 (300 mM NaOH, 1mM EDTA) at 300 mA for 40 min. Slides were washed twice in ddH2O and fixed with 70% ethanol for 5 min. Comets were stained with SYBR Safe (Invitrogen) for 30 min at room temperature. All steps were conducted in the dark to prevent additional DNA damage. Comets were analyzed using a Nikon Eclipse E600 microscope and a Nikon-DS-RI2 camera. Quantification of the Olive Tail Moment of individual nuclei was performed with the CaspLab software.

Transcriptomic analyses

RNA extraction was performed with the RNeasy Plus Micro Kit (QIAGEN) following the manufacturer's instructions. RNA samples were quantified with Qubit RNA HS Assay Kit (Thermo Fischer Scientific) and sequenced in a NovaSeq 2x150 configuration.

Raw FASTQ data underwent quality assessment using FastQC. Subsequently, reads were trimmed for adapter sequences and low-quality bases at the 3′-end with TrimGalore (v0.5.0) and aligned to the GRCh38 reference genome using STAR (v2.7.0d). The Gencode primary assembly gene transfer file (GTF) v35 served as a reference for gene annotation. Post-alignment metrics, such as coverage distribution across gene lengths and the percentage of reads mapping to exons, were gathered using Qorts (v1.3.5). Reads were assigned to genes with featureCounts (v1.6.3), considering reads that overlapped exons by at least ten nucleotides (–minOverlap 10) and excluding chimeric reads. Data preprocessing, exploratory analyses, and differential gene expression assessments were conducted using built-in functions from the DESeq2 (v1.30.0) R package. Genes with an adjusted p-value below 0.05 from the differential expression analysis were deemed differentially expressed (Table S2).

Pre-ranked gene lists based on log2 fold change (log2FC) were utilized for Gene Set Enrichment Analysis (GSEA). These analyses considered various datasets, including Gene Ontology, KEGG Pathway Database, Reactome Pathway Database, and Molecular Signatures Database v7, using built-in functions from the R package clusterProfiler (v.3.8.1). Terms with an adjusted p-value (Benjamini-Hochberg correction) of less than 0.05 were classified as significantly enriched (Table S2).

Integration site analyses

Retrieval of vector ISs

The genomic DNA from mouse-derived samples was extracted with QIAmp DNA Mini or Micro Kit (QIAGEN) and subjected to custom PCR amplification to retrieve vector ISs, the Sonication Linker mediated (SLiM)-PCR.[101,102] The SLiM-PCR was performed using the NEBNext® Ultra™ II DNA Library Prep Kit (New England Biolabs, ref: E7645) according to the manufacturer's instructions. Briefly, the procedure consists of the following steps: i) fragmentation by sonication of ~30 ng of DNA per sample; ii) splitting of each sample into three replicates; iii) end-repair, adenylation, and ligation of the fragments to a linker cassette (LC); and iv) two consecutive rounds of PCR (25 and 10 cycles of amplification, respectively) to amplify vector/cellular-genome junctions by using primers annealing to the vector genome end (Long Terminal Repeats, LTR) and the LC. Between the first and second PCRs, a clean-up and concentration step was performed to prepare the PCR product for the second reaction. The list of primers and sequences used for the SLiM-PCR procedure is reported in Table S3. Primers contain DNA barcodes, which allow univocal barcoding of all the SLiM-PCR replicates, and sequencing adapters for multiplexed paired-end sequencing on Illumina or MGI sequencers. The list of samples with the details on the applied PCR procedure and the number of reads retrieved is reported in Table S3. Two sequencing libraries composed of 267 PCR products were sequenced using the MGI DNBSEQ-G400 platform and yielded a total of >12.7x10^7 raw reads.

Identification of vector ISs

VISPA2[103] was used for the identification of ISs from PCR-amplified samples, which were sequenced using Illumina/MGI paired-end technology. In summary, for each sequencing library generated, we performed quality control filtering on paired-end reads, and

barcodes were detected to enable sample demultiplexing. Vector sequences were excised from the reads. The remaining cellular genomic sequences were aligned to the Human reference genome (GRCh37/hg19, February 2019 release). To quantify the number of genomes corresponding to each clone, we employed an estimation strategy based on the count of distinct fragments associated with each IS, utilizing the SonicLength[104] approach. This ensured that is abundance was proportionate to the initial population of contributing cells, allowing for an estimation of clonal representation in the original sample. The final set of unique ISs comprised loci that were precisely mapped and annotated with the closest RefSeq gene.

We then used ISAanalytics[105] to integrate the output files of VISPA2 and perform downstream analyses of ISs, from quality controls to the analyses of shared ISs among samples. A detailed report and code of ISAanalytics are available in the GitHub repository. We initially eliminated the occurrence of identical ISs detected across different independent samples, referred to as "collisions," following a previously established approach.[8] In brief, for the two groups of mice sharing ISs, we attributed the IS to one group if it was first identified in that one or if its relative abundance was at least ten times greater compared to the other group. The detection and resolution of collisions in independent samples were conducted using the ISAnalytics tool. We subsequently carried out quality control of the sequencing data by examining the read count for each PCR sample within each sequencing pool. Samples displaying a raw read count that was significantly under-represented (less than one-third of the average read count of other samples in the pool) were excluded from further analysis. The quality control process involved: i) the exclusion of sequencing samples with raw read counts that were three times lower than the pool's average, and ii) the elimination of potential contaminations, identified as identical ISs found in separate samples, as previously outlined.[8] For the analysis of Common Insertion Sites (CISs), we employed the Grubbs test for outlier detection[72] (as implemented in ISAnalytics). Specifically, for each mouse, we calculated the targeting frequency of individual genes based on the number of ISs located within the gene body or ±100 kb and normalized this by the gene length. After applying a log2 transformation to the distribution of gene frequencies, we conducted the Grubbs test to identify genes with targeting frequencies significantly exceeding the overall average frequency.

Population size and diversity

The estimated population size represents the number of transduced engrafting clones and was calculated as the number of unique ISs normalized on the VCN of cells at transplantation (when VCN >1, to avoid indirect estimation of untransduced clones). Population diversity was calculated using the Shannon diversity index (H-index). H-index accounts for the number of distinct species (richness) and their relative abundance with the following formula: $H' = -\sum_{i=1}^{R} p_i \ln p_i$; where i is an IS, p_i is the clonal abundance, and R is the set of clones. Several clonal studies have investigated the heterogeneity and complexity of vector-marked cells across time, tissues, and differentiated lineages, using IS as a proxy for different species and IS abundance as an indicator of species prevalence. Richness and evenness were measured over time to assess long-term efficacy (reflected by the maintenance of a high H-index) or to detect malignant events (indicated by a sharp decline in the H-index over time). The H-index was calculated using the R package vegan, incorporated into ISAnalytics, and normalized on the VCN (when VCN >1) (Table S3).

QUANTIFICATION AND STATISTICAL ANALYSIS

Measurements were taken from distinct biological samples, animals, or experiments, and the sample size (n) is indicated in the figure legends. Distinct biological samples are identified with different symbols. To adhere to the highest standards of statistical rigor, statistical comparisons were not performed when $n<5$ or for *in vitro* experiments of independently processed and transduced cells purified from the two distinct WAS patients. For paired observations, the Wilcoxon matched-pairs signed rank test was performed. The Mann-Whitney test was performed to compare two independent groups. For the *in vivo* experiment of WAS patient-derived cells, random-intercept linear mixed-effects (LME) models were used to compare biological measurements between 2D and 3D groups, either at a fixed time point within an organ or within specific cell types, depending on the context, to account for dependency among observations due to shared donors. A random effect for donor ID was specified in the model. Standard transformations (e.g., logarithmic, square root, cubic root, and ordered quantile normalization) were applied to the outcome variables to satisfy model assumptions. The Grubbs test was performed on CIS results from IS analyses. All tests were performed with two-tailed statistics. Data were analyzed using the Prism software (GraphPad Software Inc.) and R statistical software. p values <0.05 were considered significant (*, $p<0.05$; **, $p<0.01$; ***, $p<0.001$; ****, $p<0.0001$).

Cell Stem Cell, Volume *33*

Supplemental Information

Nanoengineered 3D culture substrate enables superior persistence and polyclonal engraftment of genetically engineered hematopoietic stem cells

Federico Midena, Laura Alessandrini, Claudio Conci, Matteo Barcella, Francesco Gazzo, Emanuela Jacchetti, Edoardo Carsana, Fabrizio Benedicenti, Roberta Vacca, Lucrezia della Volpe, Sergio Arévalo, Kety Giannetti, Dafne Barozzi, Martina Franchino, Erika Zonari, Francesca Ferrua, Giacomo Farina, Chiara Brombin, Federica Cugnata, Martina Fiumara, Teresa Tavella, Leonardo Cherubin, Federico Fraschetta, Giulio Cerullo, Roberto Osellame, Marina Radrizzani, Samuele Ferrari, Ivan Merelli, Bernhard Gentner, Cristina Scielzo, Andrea Brendolan, Luigi Naldini, Alessandro Aiuti, Eugenio Montini, Manuela T. Raimondi, and Raffaella Di Micco

Figure S1

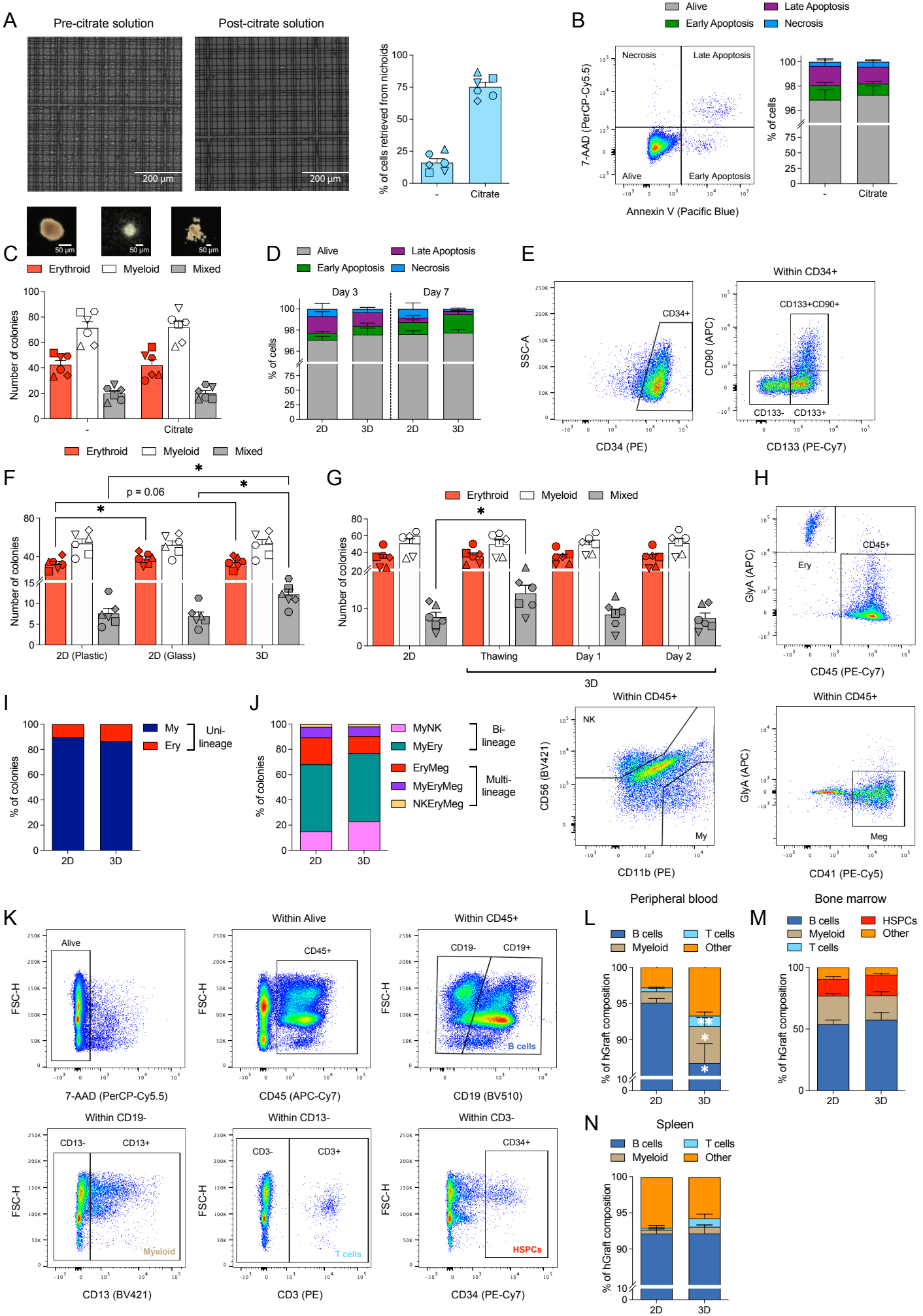
A
Pre-citrate solution
Post-citrate solution
200 µm
% of cells retrieved from nichoids
Citrate
B
Alive
Early Apoptosis
Late Apoptosis
Necrosis
7-AAD (PerCP-Cy5.5)
Annexin V (Pacific Blue)
% of cells
C
Erythroid
Myeloid
Mixed
Number of colonies
D
Day 3
Day 7
2D
3D
E
CD34+
SSC-A
CD34 (PE)
Within CD34+
CD133+CD90+
CD90 (APC)
CD133 (PE-Cy7)
F
p = 0.06
2D (Plastic)
2D (Glass)
G
Thawing
Day 1
Day 2
H
Ery
CD45+
GlyA (APC)
CD45 (PE-Cy7)
I
My
Ery
Uni-lineage
J
MyNK
MyEry
EryMeg
MyEryMeg
NKEryMeg
Bi-lineage
Multi-lineage
Within CD45+
NK
CD56 (BV421)
CD11b (PE)
Meg
CD41 (PE-Cy5)
K
Alive
FSC-H
7-AAD (PerCP-Cy5.5)
Within Alive
CD45+
CD45 (APC-Cy7)
CD19-
CD19+
B cells
CD19 (BV510)
Within CD19-
CD13-
CD13+
Myeloid
CD13 (BV421)
Within CD13-
CD3-
CD3+
T cells
CD3 (PE)
Within CD3-
CD34+
HSPCs
CD34 (PE-Cy7)
L
Peripheral blood
B cells
T cells
Myeloid
Other
% of hGraft composition
M
Bone marrow
HSPCs
N
Spleen

Figure S1. Nichoids increase the functionality of HSPCs upon *ex vivo* culture, related to Figure 1.
(A) Representative pictures of the nichoid culture substrate with CD34+ cells pre- and post-treatment with the citrate solution (left) and percentage of cells retrieved from nichoids (right) compared to conventional 2D culture. Scale bars: 200 μm.
(B) Representative gating strategy for apoptosis analysis (left). Cells are distinguished as alive (7-AAD-Annexin V-), early apoptotic (7-AAD-Annexin V+), late apoptotic (7-AAD+Annexin V+), and necrotic (7-AAD+Annexin V-). Apoptosis analysis performed within CD34+ cells (right) treated or not with the citrate solution (n=6).
(C) Representative pictures and number of erythroid, myeloid, and mixed colonies generated in the CFU-C assay from HSPCs treated or not with the citrate solution seeded on day 1 (n=6). Scale bars: 50 μm.
(D) Apoptosis analysis performed within CD34+ cells (n=6,6,5,5).
(E) Representative gating strategy for phenotypically defined HSPC subsets analysis. CD34+ cells were identified within alive cells from (A). HSPC subpopulations were discriminated as CD34+CD133-CD90-, CD34+CD133+CD90-, and primitive fraction CD34+CD133+CD90+.
(F) Number of erythroid, myeloid, and mixed colonies generated in the CFU-C assay from HSPCs seeded on day 3 upon culture in different settings (n=6). Wilcoxon test.
(G) Number of erythroid, myeloid, and mixed colonies generated in the CFU-C assay from HSPCs seeded on 2D or 3D immediately after thawing or upon one or two days after initial 2D culture (n=6). Wilcoxon test.
(H) Representative gating strategy for the HSC-enriched single-cell differentiation assay. Colonies were considered in the analysis only if >30 cells were present in the following gates: Erythroid, Ery (CD45-GlyA+); Myeloid, My (CD45+CD11b+); Natural Killer, NK (CD45+CD56+CD11b-); Megakaryocyte, Meg (CD45+CD41+GlyA-).
(I,J) Percentage of different lineages within uni-lineage (I) or bi/multi-lineage (J) colonies generated in the single-cell differentiation assay.
(K) Representative gating strategy for PB, BM, and SP analyses. hCD45+ cells were identified within alive cells (7-AAD-). Within the human graft, cells were discriminated as B cells (CD45+CD19+), myeloid cells (CD45+CD19-CD13+), T cells (CD45+CD19-CD13-CD3+), HSPCs (CD45+CD19-CD13-CD3-CD34+) or other (CD45+CD19-CD13-CD3-CD34-).
(L-N) Percentage of human graft composition in the PB (L), BM (M), and SP (N) at the endpoint of transplanted mice (n=5). Mann-Whitney test.
Mean ± SEM. *$p < 0.05$; **$p < 0.01$.

Figure S2

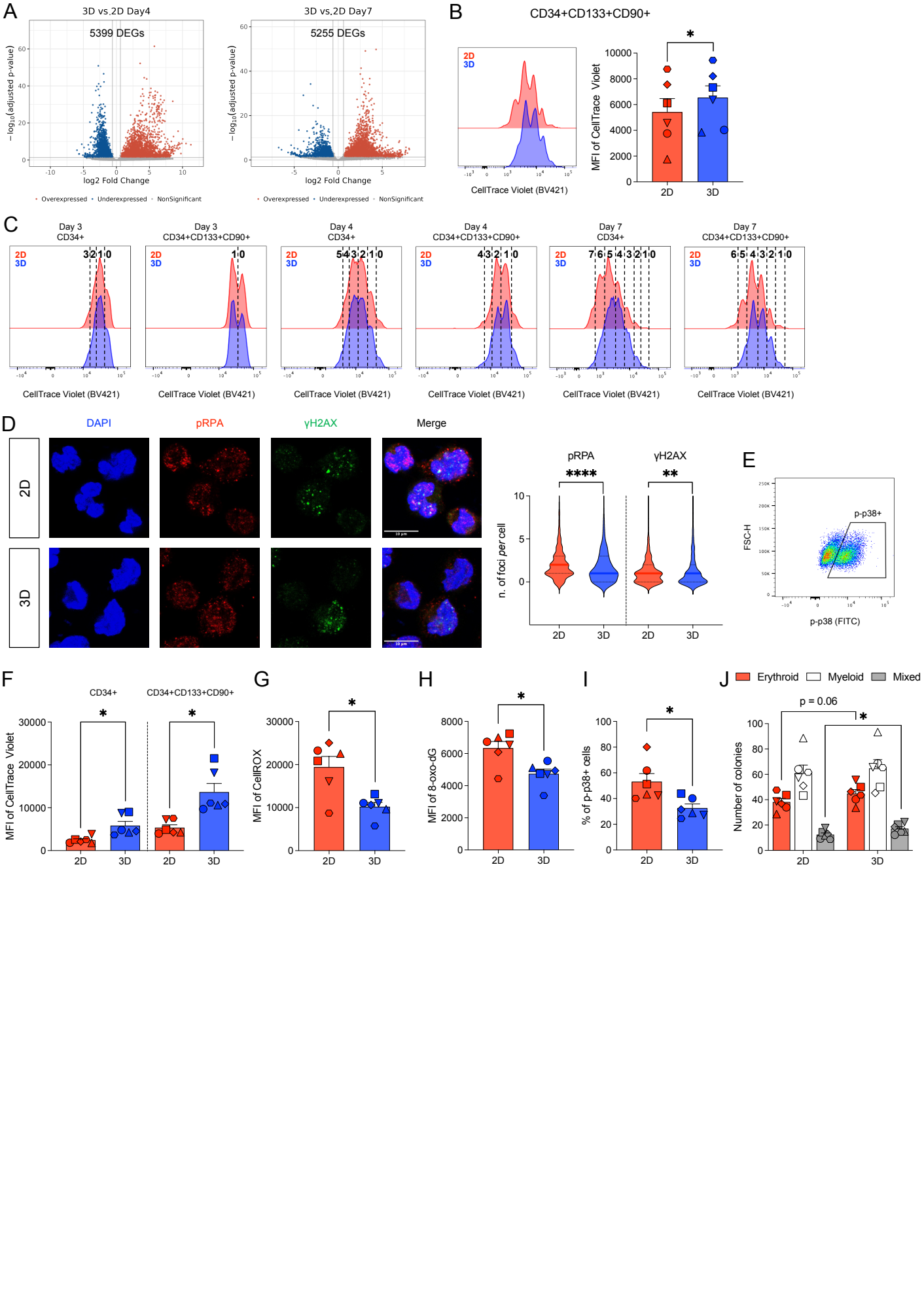
A
3D vs.2D Day4
5399 DEGs
3D vs.2D Day7
5255 DEGs
log2 Fold Change
Overexpressed
Underexpressed
NonSignificant
B
CD34+CD133+CD90+
2D
3D
CellTrace Violet (BV421)
MFI of CellTrace Violet
C
Day 3 CD34+
Day 3 CD34+CD133+CD90+
Day 4 CD34+
Day 4 CD34+CD133+CD90+
Day 7 CD34+
Day 7 CD34+CD133+CD90+
D
DAPI
pRPA
γH2AX
Merge
n. of foci per cell
E
p-p38+
FSC-H
p-p38 (FITC)
F
CD34+
CD34+CD133+CD90+
MFI of CellTrace Violet
G
MFI of CellROX
H
MFI of 8-oxo-dG
I
% of p-p38+ cells
J
Erythroid
Myeloid
Mixed
p = 0.06
Number of colonies

Figure S2. Nichoids remodel HSPC gene expression, reducing cell proliferation and DNA damage accumulation, related to Figure 2.

(A) Differentially expressed genes (FDR < 0.05) in 3D- vs. 2D-cultured HSPCs.

(B) Representative plot (left) and MFI (right) of CellTrace dye dilution on day 7 (n=6) in the HSC-enriched subset. Wilcoxon test.

(C) Representative plot of CellTrace dye dilution over time in bulk and HSC-enriched subsets. Values indicate the number of cell divisions performed by each cell in the highlighted peaks.

(D) Representative immunofluorescence staining (left) of DAPI (blue), pRPA (red), and γH2AX (green) and number of DDR foci (right) per cell (more than 800 cells were analyzed for each condition). Median. Mann-Whitney test. Scale bars: 10 μm.

(E) Representative gating strategy for p-p38 analyses.

(F) MFI of CellTrace dye dilution in bulk and HSC-enriched subsets on day 7 from freshly-isolated CB-derived HSPCs (n=6). Wilcoxon test.

(G) MFI of ROS measured by CellROX staining on day 7 from freshly-isolated CB-derived HSPCs (n=6). Wilcoxon test.

(H) MFI of 8-oxo-dG on day 7 from freshly-isolated CB-derived HSPCs (n=6). Wilcoxon test.

(I) Percentage of phospho-p38 (p-p38)-positive cells on day 7 from freshly-isolated CB-derived HSPCs (n=6). Wilcoxon test.

(J) Number of erythroid, myeloid, and mixed colonies generated in the CFU-C assay from freshly-isolated CB-derived HSPCs seeded on day 7 (n=6). Wilcoxon test.

Unless otherwise specified, Mean ± SEM. *p < 0.05; **p < 0.01; ****p < 0.0001.

Figure S3

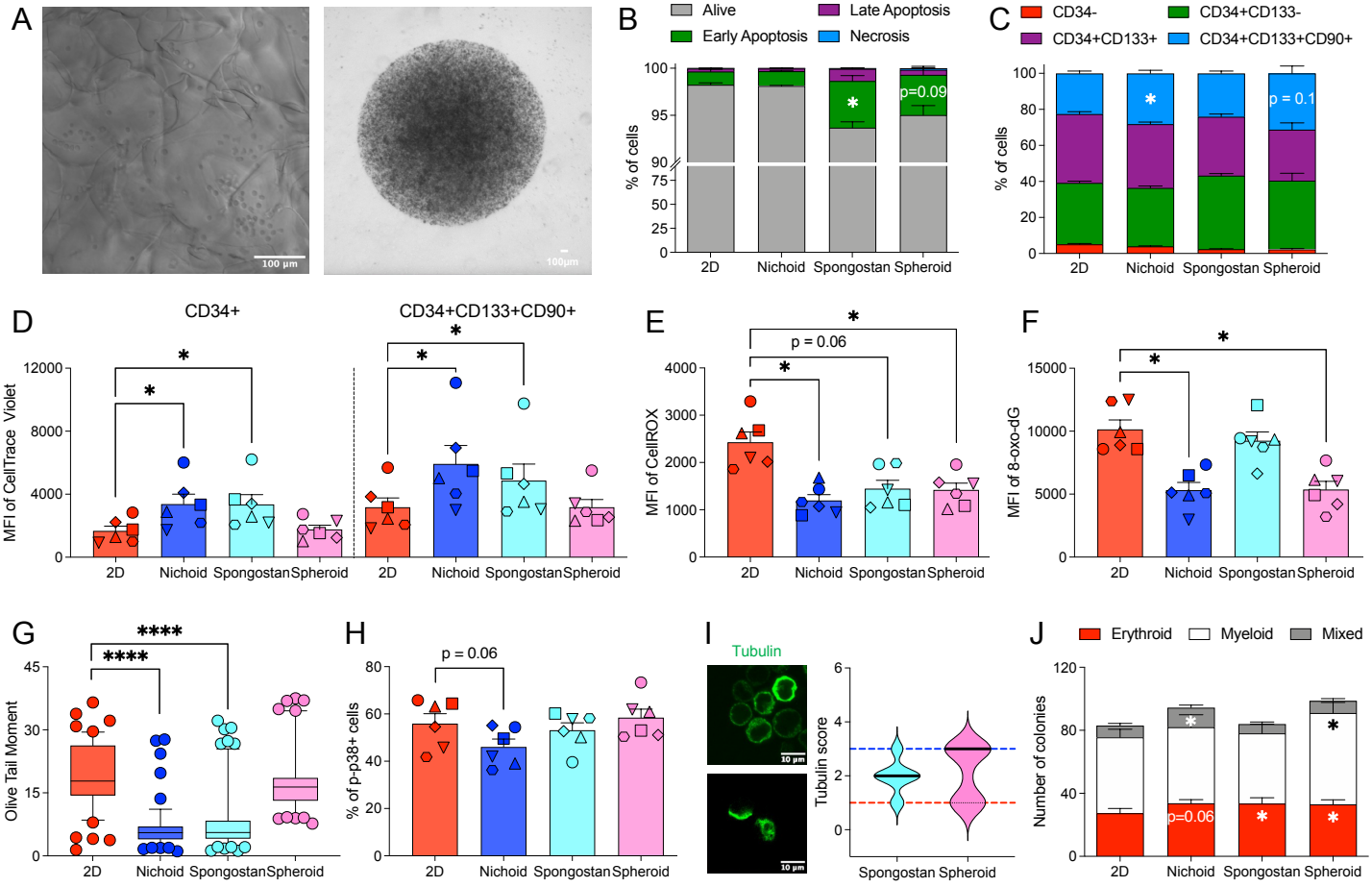
A
100 µm
100µm
B
Alive
Early Apoptosis
Late Apoptosis
Necrosis
% of cells
p=0.09
2D
Nichoid
Spongostan
Spheroid
C
CD34-
CD34+CD133+
CD34+CD133-
CD34+CD133+CD90+
% of cells
p = 0.1
D
CD34+
CD34+CD133+CD90+
MFI of CellTrace Violet
E
p = 0.06
MFI of CellROX
F
MFI of 8-oxo-dG
G
Olive Tail Moment
H
p = 0.06
% of p-p38+ cells
I
Tubulin
Tubulin score
J
Erythroid
Myeloid
Mixed
Number of colonies
p=0.06

Figure S3. Distinct 3D culture platforms may differentially regulate HSPC responses, related to Figure 2.

(A) Representative pictures of CD34+ cells cultured in spongostan scaffolds (left) and collagen-based spheroids (right). Scale bars: 100 μm.

(B) Apoptosis analysis performed within CD34+ cells on day 7 (n=6).

(C) Percentage of phenotypically defined HSPC subsets on day 7 (n=6).

(D) MFI of CellTrace dye dilution in bulk and HSC-enriched subsets on day 7 (n=6). Wilcoxon test.

(E) MFI of ROS measured by CellROX staining in HSPCs on day 7 (n=6). Wilcoxon test.

(F) MFI of 8-oxo-dG in HSPCs on day 7 (n=6). Wilcoxon test.

(G) Quantification of single-strand and double-strand breaks by alkaline comet assay on day 7; each dot represents a single cell (more than 100 cells were analyzed for each condition). Median ± 95% CI. Mann-Whitney test.

(H) Percentage of phospho-p38 (p-p38)-positive HSPCs on day 7 (n=6). Wilcoxon test.

(I) Representative immunofluorescence (left) showing tubulin spatial organization in HSPCs in spongostan scaffolds (top) and collagen-based spheroids (bottom), and tubulin score (right) on day 7. Dashed lines represent the tubulin score of HSPCs cultured in 2D (red) and nichoid (blue). Median Value. Mann-Whitney test. Scale bars: 10 μm.

(J) Number of erythroid, myeloid, and mixed colonies generated in the CFU-C assay from HSPCs seeded on day 7 (n=6). Wilcoxon test.

Unless otherwise specified, Mean ± SEM. *$p < 0.05$; **$p < 0.01$; ****$p < 0.0001$.

Figure S4

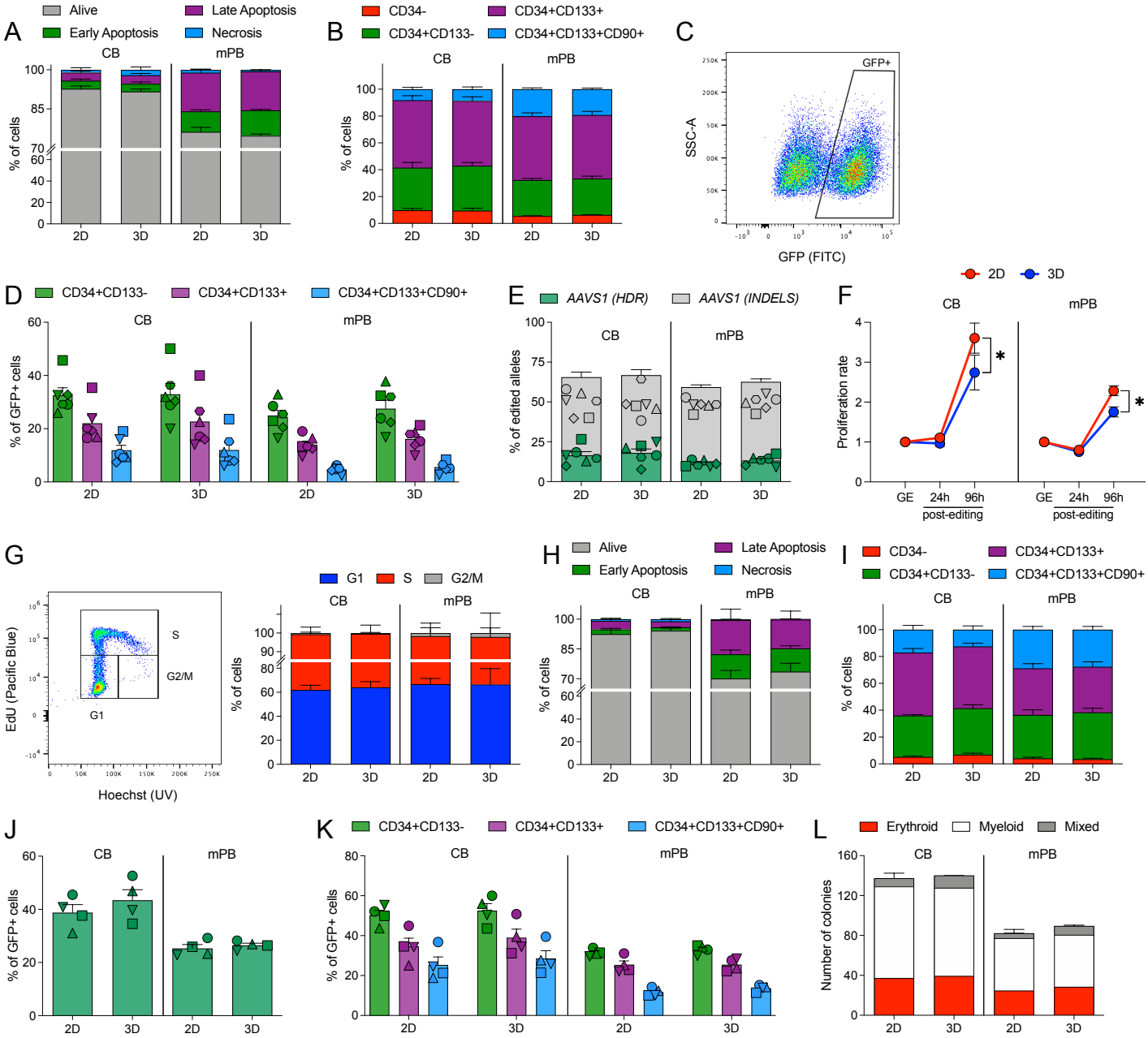
A
Alive
Late Apoptosis
Early Apoptosis
Necrosis
CB
mPB
% of cells
2D
3D
B
CD34-
CD34+CD133+
CD34+CD133-
CD34+CD133+CD90+
C
GFP+
SSC-A
GFP (FITC)
D
CD34+CD133-
CD34+CD133+
CD34+CD133+CD90+
% of GFP+ cells
E
AAVS1 (HDR)
AAVS1 (INDELS)
% of edited alleles
F
2D
3D
Proliferation rate
GE
24h
96h
post-editing
G
G1
S
G2/M
EdU (Pacific Blue)
Hoechst (UV)
H
I
J
K
L
Erythroid
Myeloid
Mixed
Number of colonies

Figure S4. Nichoids enable efficient long-range gene editing, related to Figure 3.
(A) Apoptosis analysis performed within CD34+ cells on day 4 (n=6).
(B) Percentage of phenotypically defined HSPC subsets on day 4 (n=6).
(C) Representative gating strategy for editing efficiency analysis. GFP+ cells were identified within CD34+ cells (gated within alive cells).
(D) Percentage of edited cells within HSPC subsets on day 7 (n=6).
(E) Percentage of edited alleles by HDR or non-homologous end joining (NHEJ) in HSPCs on day 7 (n=6).
(F) Proliferation rate of HSPCs upon GE (GE=day 3, 24h post-editing=day 4, 96h post-editing=day 7). (n=6). Wilcoxon test (calculated at the last time point).
(G) Representative plot (left) and percentage of HSPCs in indicated cell cycle phases (right) on day 3 (before GE) (n=4).
(H) Apoptosis analysis performed within CD34+ cells on day 4 edited with Cas9/AAV6 plus GSE56 and Ad5-E4orf6/7 editing enhancers (n=4).
(I) Percentage of phenotypically defined HSPC subsets on day 4 in cells edited with Cas9/AAV6 plus GSE56 and Ad5-E4orf6/7 editing enhancers (n=4).
(J,K) Percentage of GFP+ cells in bulk (J) and HSPC subsets (K) on day 7 from cells edited with Cas9/AAV6 plus GSE56 and Ad5-E4orf6/7 editing enhancers (n=4).
(L) Number of erythroid, myeloid, and mixed colonies generated in the CFU-C assay from cells edited with Cas9/AAV6 plus GSE56 and Ad5-E4orf6/7 editing enhancers seeded on day 4 (n=4).
Mean ± SEM. *$p < 0.05$.

Figure S5

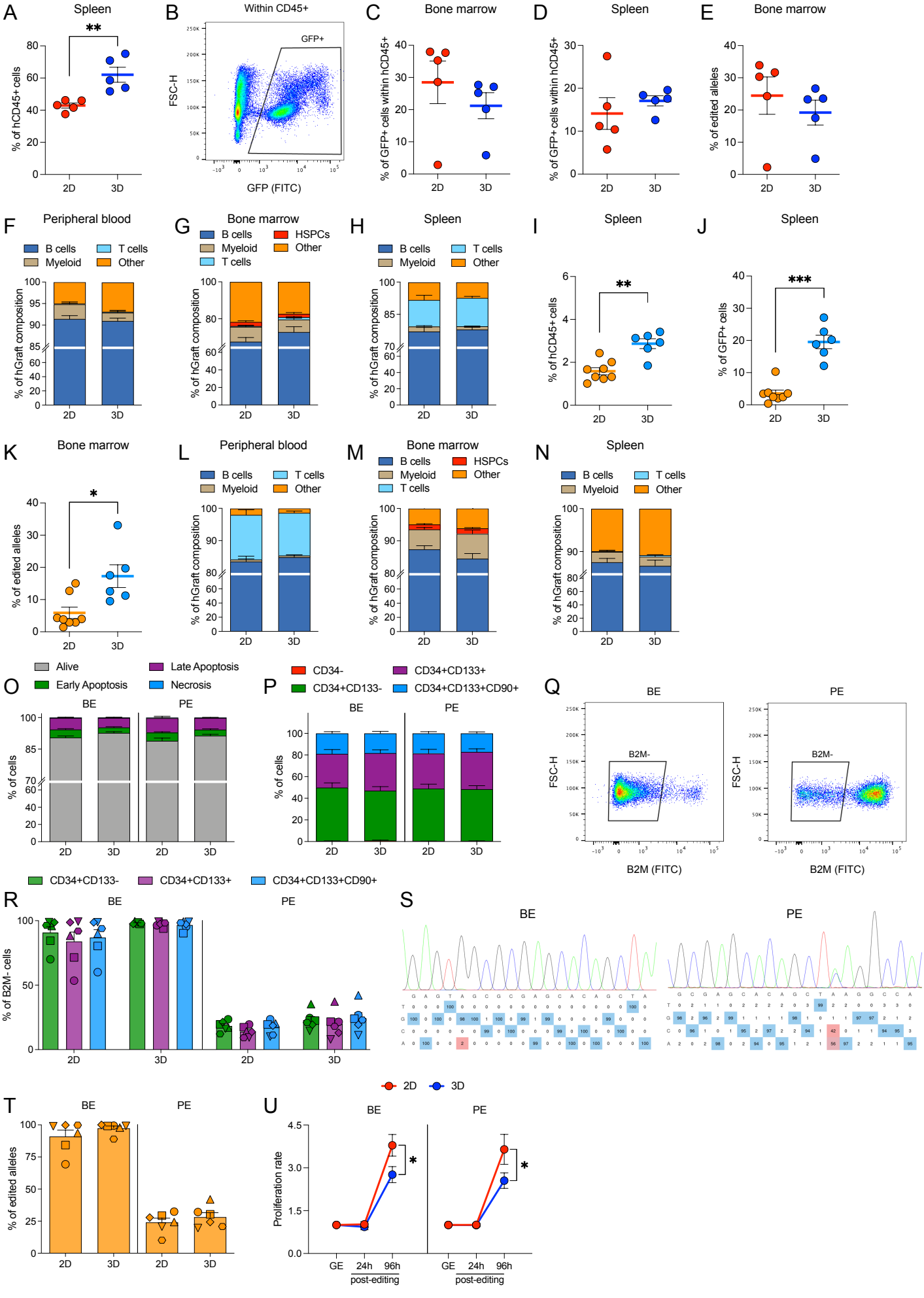
A
Spleen
% of hCD45+ cells
2D
3D
B
Within CD45+
GFP+
FSC-H
GFP (FITC)
C
Bone marrow
% of GFP+ cells within hCD45+
D
Spleen
% of GFP+ cells within hCD45+
E
Bone marrow
% of edited alleles
F
Peripheral blood
B cells
T cells
Myeloid
Other
% of hGraft composition
G
Bone marrow
HSPCs
H
Spleen
I
Spleen
% of hCD45+ cells
J
Spleen
% of GFP+ cells
K
Bone marrow
% of edited alleles
L
Peripheral blood
M
Bone marrow
N
Spleen
Alive
Late Apoptosis
Early Apoptosis
Necrosis
O
BE
PE
% of cells
P
CD34-
CD34+CD133+
CD34+CD133-
CD34+CD133+CD90+
Q
BE
PE
B2M-
FSC-H
B2M (FITC)
CD34+CD133-
CD34+CD133+
CD34+CD133+CD90+
R
BE
PE
% of B2M- cells
S
BE
PE
T
BE
PE
% of edited alleles
2D
3D
U
BE
PE
Proliferation rate
GE
24h
96h
post-editing

Figure S5. Nichoids allow efficient GE across multiple engineering platforms and improve the engraftment of HDR-edited cells in serial transplantation experiments, related to Figure 3.
(A) Percentage of hCD45+ cells measured in the SP at the endpoint of transplanted mice (n=5). Mann-Whitney test.
(B) Representative gating strategy for GFP analyses in xenotransplantation experiments.
(C,D) Percentage of GFP+ cells (within hCD45+ cells) in the BM (C) and SP (D) at the endpoint of transplanted mice (n=5).
(E) Percentage of HDR-edited alleles by HDR from human cells measured in the BM at the endpoint of transplanted mice (n=5).
(F-H) Percentage of human graft composition in the PB (F), BM (G), and SP (H) at the endpoint of transplanted mice (n=5).
(I,J) Percentage of hCD45+ cells (I) and GFP+ cells (within hCD45+ cells) (J) measured in the SP at the endpoint of transplanted secondary recipients (n=8,6). Mann-Whitney test.
(K) Percentage of HDR-edited alleles by HDR from human cells measured in the BM at the endpoint of transplanted secondary recipients (n=8,6).
(L-N) Percentage of human graft composition in the PB (L), BM (M), and SP (N) at the endpoint of transplanted secondary recipients (n=8,6).
(O) Apoptosis analysis performed within CD34+ cells on day 4 edited with BE or PE (n=6).
(P) Percentage of phenotypically defined HSPC subsets on day 4 in cells edited with BE or PE (n=6).
(Q) Representative gating strategy for editing efficiency analysis. B2M-negative cells were identified within CD34+ cells (gated within alive cells).
(R) Percentage of B2M- cells within HSPC subsets on day 7 (n=6).
(S) Representative Sanger Sequencing data from base- (left) and prime-edited cells on day 7 (right).
(T) Percentage of edited alleles on day 7 by Sanger Sequencing in HSPCs edited with BE or PE (n=6).
(U) Proliferation rate of HSPCs upon GE with BE or PE (GE=day 3, 24h post-editing=day 4, 96h post-editing=day 7). (n=6). Wilcoxon test (calculated at the last time point).
Mean ± SEM. *$p < 0.05$; **$p < 0.01$; ***$p < 0.001$.

Figure S6

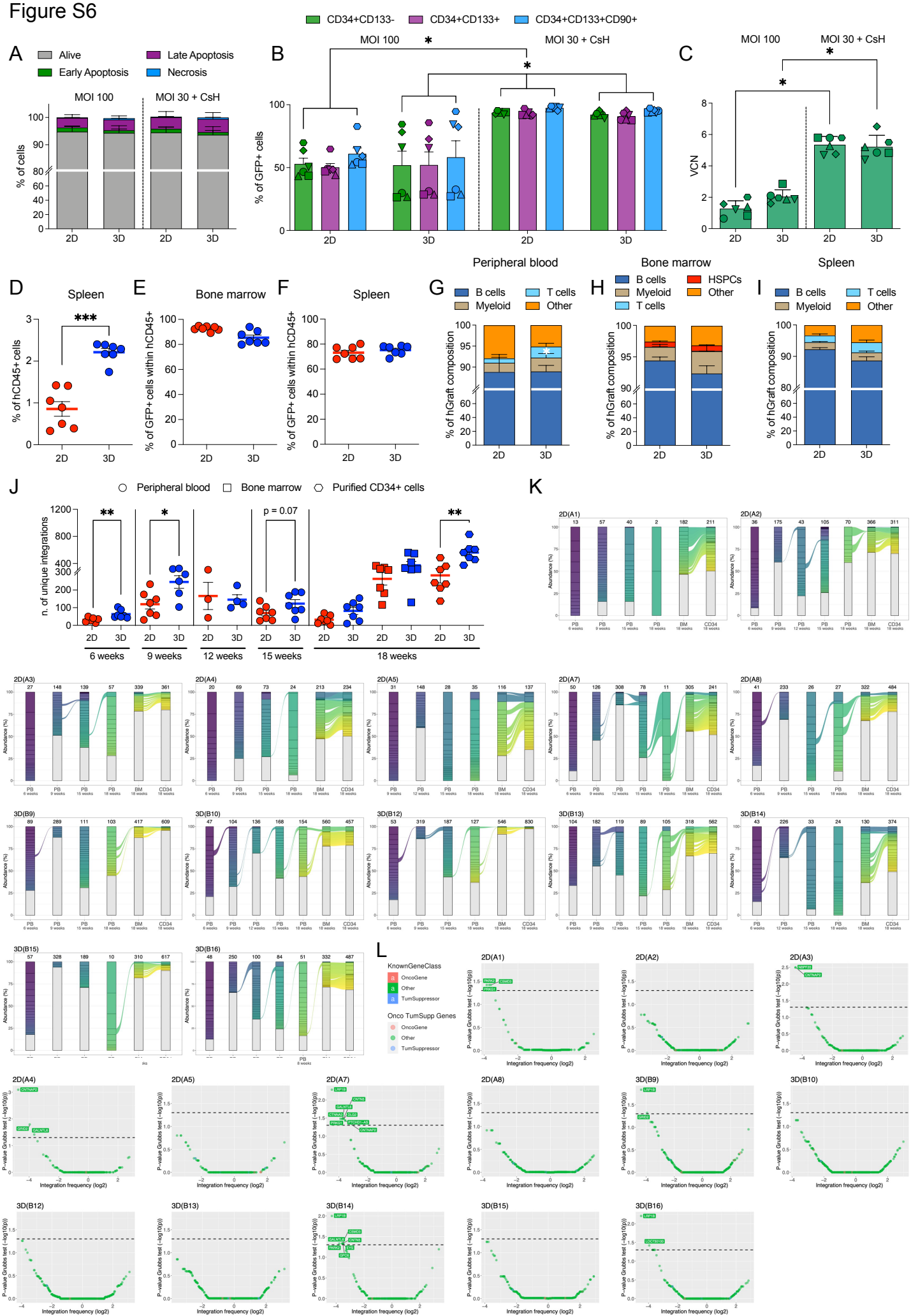
A
Alive
Early Apoptosis
Late Apoptosis
Necrosis
MOI 100
MOI 30 + CsH
% of cells
2D
3D
B
CD34+CD133-
CD34+CD133+
CD34+CD133+CD90+
MOI 100
MOI 30 + CsH
% of GFP+ cells
C
MOI 100
MOI 30 + CsH
VCN
D
Spleen
% of hCD45+ cells
E
Bone marrow
% of GFP+ cells within hCD45+
F
Spleen
% of GFP+ cells within hCD45+
Peripheral blood
Bone marrow
Spleen
G
B cells
Myeloid
T cells
Other
% of hGraft composition
H
B cells
Myeloid
T cells
HSPCs
Other
% of hGraft composition
I
B cells
Myeloid
T cells
Other
% of hGraft composition
J
Peripheral blood
Bone marrow
Purified CD34+ cells
n. of unique integrations
p = 0.07
6 weeks
9 weeks
12 weeks
15 weeks
18 weeks
K
2D(A1)
2D(A2)
2D(A3)
2D(A4)
2D(A5)
2D(A7)
2D(A8)
3D(B9)
3D(B10)
3D(B12)
3D(B13)
3D(B14)
3D(B15)
3D(B16)
Abundance (%)
PB 6 weeks
PB 9 weeks
PB 12 weeks
PB 15 weeks
PB 18 weeks
BM 18 weeks
CD34 18 weeks
L
KnownGeneClass
OncoGene
Other
TumSuppressor
Onco TumSupp Genes
OncoGene
Other
TumSuppressor
P-value Grubbs test (-log10(p))
Integration frequency (log2)
2D(A1)
2D(A2)
2D(A3)
2D(A4)
2D(A5)
2D(A7)
2D(A8)
3D(B9)
3D(B10)
3D(B12)
3D(B13)
3D(B14)
3D(B15)
3D(B16)

Figure S6. Nichoids enable efficient LV-mediated gene addition, related to Figure 4.
(A) Apoptosis analysis performed within CD34+ cells on day 2 (n=3).
(B) Percentage of GFP+ cells within HSPC subsets on day 10 (n=6). Wilcoxon test.
(C) VCN of transduced HSPCs on day 10 (n=6). Wilcoxon test.
(D) Percentage of hCD45+ cells measured in the SP at the endpoint of transplanted mice (n=7). Mann-Whitney test.
(E,F) Percentage of GFP+ cells (within hCD45+ cells) in the BM (E) and SP (F) at the endpoint of transplanted mice (n=7).
(G-I) Percentage of human graft composition in the PB (G), BM (H), and SP (I) at the endpoint of transplanted mice (n=7). Mann-Whitney test.
(J) Number of unique integrations from IS analyses. Mann-Whitney test.
(K) Tracking and relative abundance of ISs reported over time in transplanted mice (A=2D group, B=3D group). Each colored bar univocally identifies an IS with >1% representation in at least one time point, with its abundance proportional to the height of the bar; a colored ribbon connects two neighboring time points for each recaptured clone. The total number of unique ISs is reported on each bar.
(L) IS gene frequency and CIS analysis in transplanted mice (A=2D group, B=3D group). Each dot represents a gene, labeled with the corresponding color if observed as significant. The dashed line is the alpha value 0.05. Grubbs test.
Mean ± SEM. *$p < 0.05$; **$p < 0.01$; ***$p < 0.001$.

Figure S7

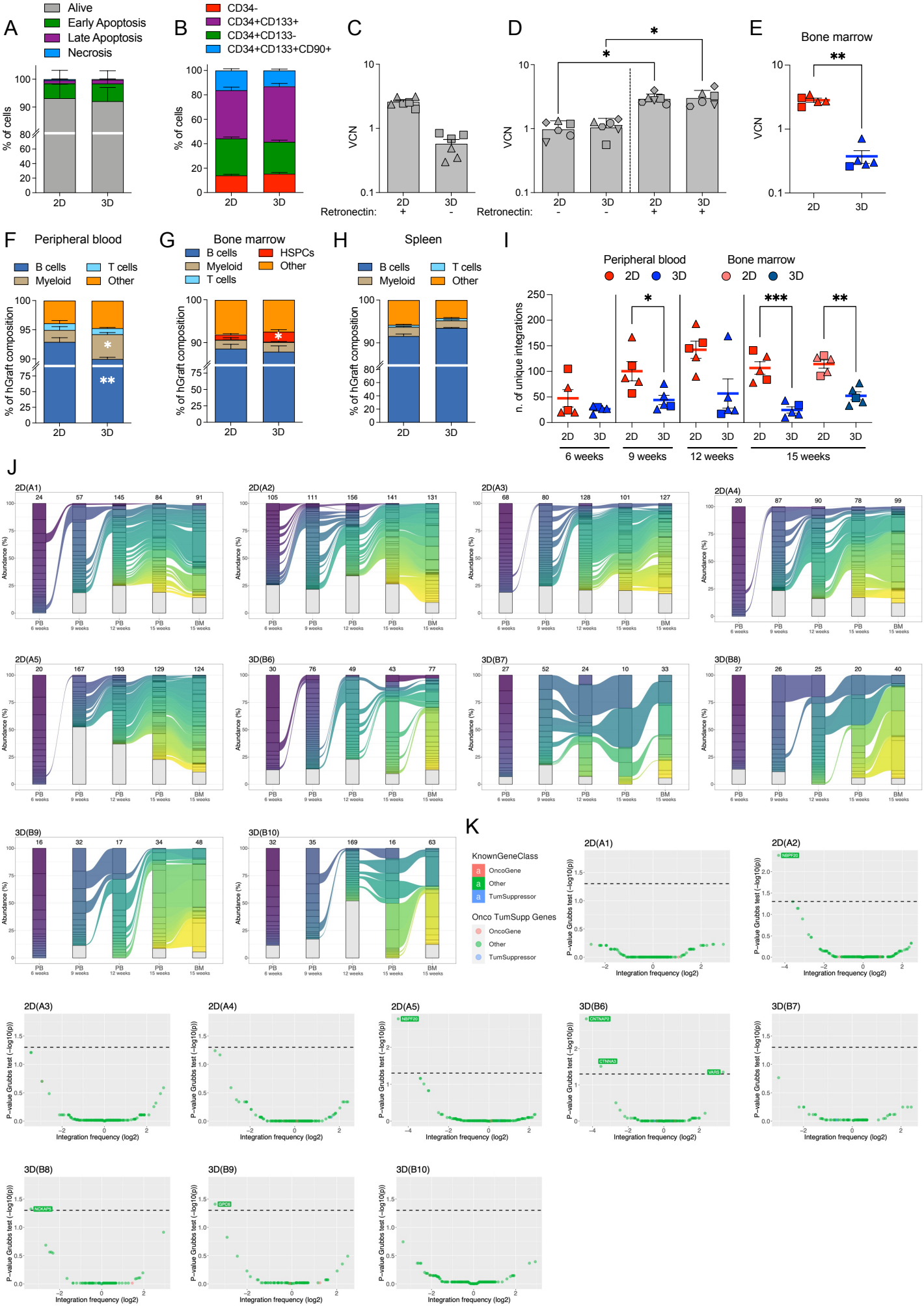
A
Alive
Early Apoptosis
Late Apoptosis
Necrosis
% of cells
2D
3D
B
CD34-
CD34+CD133+
CD34+CD133-
CD34+CD133+CD90+
% of cells
C
VCN
Retronectin:
D
VCN
Retronectin:
E
Bone marrow
VCN
F
Peripheral blood
B cells
T cells
Myeloid
Other
% of hGraft composition
G
Bone marrow
B cells
HSPCs
Myeloid
Other
T cells
% of hGraft composition
H
Spleen
B cells
T cells
Myeloid
Other
% of hGraft composition
I
Peripheral blood
Bone marrow
2D
3D
n. of unique integrations
6 weeks
9 weeks
12 weeks
15 weeks
J
2D(A1)
2D(A2)
2D(A3)
2D(A4)
2D(A5)
3D(B6)
3D(B7)
3D(B8)
3D(B9)
3D(B10)
Abundance (%)
PB 6 weeks
PB 9 weeks
PB 12 weeks
PB 15 weeks
BM 15 weeks
K
KnownGeneClass
OncoGene
Other
TumSuppressor
Onco TumSupp Genes
OncoGene
Other
TumSuppressor
2D(A1)
2D(A2)
2D(A3)
2D(A4)
2D(A5)
3D(B6)
3D(B7)
3D(B8)
3D(B9)
3D(B10)
P-value Grubbs test (-log10(p))
Integration frequency (log2)
NBPF20
CNTNAP2
CTNNA3
VARS2
NCKAP5
SPC5

Figure S7. Nichoids increase the engraftment and clonal complexity of WAS patient-derived HSPCs upon gene addition, related to Figure 5.
(A) Apoptosis analysis performed within CD34+ cells on day 3 (n=6).
(B) Percentage of phenotypically defined HSPC subsets on day 3 (n=6).
(C) VCN of transduced HSPCs on day 10 (n=6).
(D) VCN of transduced HSPCs from healthy donors according to the transduction protocol described in Figure 5A, in the presence or absence of retronectin (n=6). Wilcoxon test.
(E) VCN of human cells measured in the BM at the endpoint of transplanted mice (n=5). Random-intercept LME model.
(F-H) Percentage of human graft composition in the PB (F), BM (G), and SP (H) at the endpoint of transplanted mice (n=5). Random-intercept LME models.
(I) Number of unique integrations from IS analyses. Random-intercept LME model.
(J) Tracking and relative abundance of ISs reported over time in transplanted mice (A=2D group, B=3D group). Each colored bar univocally identifies an IS with >1% representation in at least one time point, with its abundance proportional to the height of the bar; a colored ribbon connects two neighboring time points for each recaptured clone. The total number of unique ISs is reported on each bar.
(K) IS gene frequency and CIS analysis in transplanted mice (A=2D group, B=3D group). Each dot represents a gene, labeled with the corresponding color if observed as significant. The dashed line is the alpha value 0.05. Grubbs test.
Mean ± SEM. *$p < 0.05$; **$p < 0.01$; ***$p < 0.001$.